



MSc Physics and Astronomy

Track Advanced Matter and Energy Physics

Master thesis

Towards quantum simulation with two-dimensional trapped ion crystals

Implementing controllable laser systems and trap
characterization

by

Zhenlin Wu

ID 12589608

July 2021

60EC, 2020-2021

Daily Supervisor:
Matteo Mazzanti

Examiner:
Dr. Rene Gerristma
Dr. Robert Spreeuw

Abstract

Two-dimensional trapped ion quantum systems can be used for quantum simulation of various spin models. In these systems, spin-spin interactions are mediated by phonons in the ion crystal driven by state-dependent laser force. By applying optical tweezers that modify the phonon mode structure of an ion crystal, the spin-spin interaction configuration can be further engineered to emulate more intriguing spin systems. In this thesis, we describe the experimental setup built towards the realization of two-dimensional trapped ion quantum simulation with optical tweezers, including the vacuum system, the ion trap, the lasers for photoionizing and Doppler cooling the ions, and the imaging system with the optical tweezers implementation. We discuss the control systems of the lasers and trap voltages that involve relevant software and hardware development. At the end of the thesis, we present the results for preliminary trap characterization based on trap frequency measurements and the observation of two-dimensional $^{174}\text{Yb}^+$ ion crystals in the trap.

Acknowledgments

First and foremost, I would like to thank my supervisor Dr. Rene Gerristma for offering me the opportunity to participate in the 2D ion crystal project at the HyQS group. I have learnt a lot from in this newborn experiment and I always feel pleasant to work here with the group members for their kindness and support. I shall miss all the lunch and coffee time we spent together.

I would like to thank Eleanor Trimby, Henrik Hirzler and Dr. Rianne Lous from the Li – Yb⁺ experiment, for all the daily discussions and help. Henrik is also the advisor for my short-term project and the teaching assistant for my Quantum Optics course who shows me all the basics. I'm always motivated by his passion for the experiment. Coming from non English speaking environment, I was also able to improve my oral English a lot from our conversation the first few months. Besides, I would like to thank Dr. Arghavan Safavi-Naini, our theory PI, for the inspiring discussions about optical tweezer experiments during the meeting. For the 2D experiment side, I want to thank Juan Diego Arias Espinoza, our knowledgeable theorist. I really enjoy our discussions and benefit a lot from his kind suggestions. I shall also thank our postdoc, Dr. Rima Schüssler, a professional researcher and a warmhearted person and I will always remember the days we worked together in the experiment. Congratulations and best wishes for your marriage!

And I should of course thank Matteo Mazzanti, my daily supervisor, as well as the best lab buddy and friend. It would be hard to go through all the time we spent together and list all the help I got from him in terms of study and life. It is really a pity that we could not push forward the experiment together and I wish all the best for your project and career. I will miss your Tiramisu and lengthy explanations.

During my project, I have also benefit from many other skilled and helpful people outside the group. Dr. Shayne Bennetts, Dr. Stefan Alaric Schäffer and the iqClock team offer us a lot of help in terms of equipment and advice for the optical reference cavity. Dr. Shayne Bennetts and Dr. Benjamin Pasquiou also help us greatly for baking the vacuum chamber. For implementing the Red Pitaya device in the cavity lock, I have benefited a lot from the discussion with Premjith Thekkeppat and Thies Plassmann. Former member of the group, Dr. Norman V. Ewald and Dr. Thomas Feldker, also provide useful information for building the cavity and the vacuum system. Prof. Klaasjan van Druten offers kind support during the relocation of the experiment in the new lab. I would like to express sincere gratitude to people from the Technology Centre of the University of Amsterdam. They are experts for electronics, machining and glass manufacturing and contribute significantly in all aspects of the experiment.

Furthermore, I would like to thank Francesca Famà, Rodrigo González Escudero and Camila Beli Silva for the good time we spent together.

In the end, I need to thank my friends in China and my parents, especially my mother, for their love and support.

Contents

1	Introduction	2
1.1	Outline of contents	3
2	Theory of Ion Trapping	5
2.1	Paul trap confinement	5
2.2	Ytterbium ion qubit	7
2.3	Spin-spin interaction	8
3	Experimental Setup	12
3.1	Vacuum system	12
3.2	Ion Trap	14
3.2.1	Trap configuration	14
3.2.2	Electrode connection	15
3.3	Photoionization	17
3.4	Laser configuration	20
3.4.1	369 nm Doppler setup	22
3.4.2	935 nm Repumper setup	23
3.4.3	760 nm Repumper setup	24
3.5	Imaging and optical tweezers	25
4	System Control	27
4.1	Laser control	27
4.1.1	Power control based on AOM	27
4.1.2	Frequency Locking on cavity	29
4.1.3	Frequency locking on wavemeter	33
4.2	Trap voltage control	35
4.2.1	Master control program	35
4.2.2	Iseg module control	36
5	Trap Characterization	38
5.1	Trap frequency measurements	38
5.2	Magnification of imaging system	40
5.3	Generation of 2D crystals	40
6	Conclusion and Outlook	43
A	ECDL Circuits	44
B	Shutter Control Codes	47
	Bibliography	49

Chapter 1

Introduction

Quantum information processing and quantum simulation are believed to trigger future breakthroughs in various influential fields like material design and drug development [1–4]. Quantum information theory provides the blueprint for universal quantum computation that utilizes the exponentially growing complexity of entangled quantum bit (qubit) systems and has unprecedented computing capability based on quantum parallelism [5]. However, functional quantum computation requires considerable amount of qubits with error bounded operations [6–8]. In comparison, quantum simulation can be performed on small-scale controllable quantum systems and can effectively emulate the behaviour of interesting quantum systems that requires significant computing power with classical methods [9, 10].

Trapped ions have emerged for decades as one of the most promising candidates for quantum information processing [11–14] and also quantum simulation [10, 15–18]. In this type of system, atomic levels of the ions captured by electromagnetic field are used as qubits and the states of qubits can be manipulated with lasers or microwaves. Under laser cooling, the ions in the trap are stabilized to certain crystal configuration based on Coulomb interactions and trap confinement. An N -ion crystal has $3N$ vibrational phonon modes at different frequencies, reflecting the correlation between the motions of the ions. By qubit state dependently exciting these phonon modes, entanglement between the qubits can be generated. A typical way of realizing this on two ions is the so-called Mølmer-Sørensen scheme [13], which uses two pairs of Raman lasers driving the qubit transition with opposite detuning $\pm\mu$ and sufficiently close to the sidebands related to a certain vibrational mode. When the detuning μ is far from all the vibrational mode frequencies, the off-resonant coupling generates spin-spin interactions between the ions which are ideal for quantum simulation of spin systems [16, 19]. For ions in 2D configurations instead of a 1D chain, intriguing 2D quantum magnetic models can be simulated [17].

However, although the spin-spin interactions can be tuned by varying the detuning μ , the tunability of the interaction configuration is limited, which places restrictions on the type of systems that can be simulated. To address this, we intend to introduce optical tweezers on trapped ions that provide tunable local pinning curvatures for each ion. This results in more significant tuning of the vibrational modes of the ion crystal and thus a more powerful quantum simulator with more accessible spin-spin interaction configurations [20].

The group has started building the setup for implementing the optical tweezer trapped ion quantum simulator in 2018. In my master project, I have built the external cavity diode laser for photoionizing Yb atoms and the optical setups for the Doppler cooling and repumping of the ions. I have also designed and implemented the control of the laser beams based on mechanical shutters and acoustic-optical modulators, and programmed the locking of the photoionization and Doppler cooling lasers on a wavemeter. For frequency stabilization of the 760 nm repumper laser, I have modified a homebuilt optical reference cavity and implemented the Pound-Drever-Hall locking of the laser frequency to it. In collaboration with Matteo Mazzanti and Dr. Rima Schüssler, I have also worked on the vacuum system for the ion trap and programmed the control system of the trap voltages.

As a summary for my master project, this thesis describes the established experimental setup for realizing a trapped ion quantum simulator, including preliminary characterization of system. As is shown in the thesis, the system can now be used to trap and Doppler cool $^{174}\text{Yb}^+$ ions and to generate 2D ion crystals.

1.1 Outline of contents

The thesis is organized as follows: in Chapter 2, the basic theory of ion trapping in a quadrupole ion trap is presented, along with the theoretical description of using the qubit transition in $^{171}\text{Yb}^+$ ions for quantum simulation. The idea of engineering spin-spin interactions in 2D ion crystals with optical tweezers will also be discussed. In Chapter 3, our experimental setup will be described in details, including the vacuum system, the ion trap inside and the electronics connection to it, the photoionization system that produces the ions, the laser setups involved in Doppler cooling the trapped ions, and the imaging system of the ions where optical tweezers are also applied. In Chapter 4, various control systems of the experiment will be discussed. For the lasers, a description of the laser power control with acoustic-optical modulators and the laser frequency stabilization on either an optical reference cavity or a wavemeter will be given. The programming for trap voltages control on the Master Control Program will also be described. In Chapter 5, the results of preliminary trap characterizations will be presented and

discussed, which includes the axial and radial trap frequencies measurements, the estimation of the magnification of our imaging system and the effect of the high voltage DC electrodes used for generating 2D ion crystals.

Chapter 2

Theory of Ion Trapping

2.1 Paul trap confinement

As stated by Earnshaw's theorem [21], stable confinement of a charged particle, in our case a single ion, cannot be achieved by merely using static electric fields since the field potential has to be divergenceless and cannot have local minima in all three directions. However, by switching between different field configurations, it is possible to realize effective trapping of an ion. This idea led to the invention of the so-called Paul trap by Wolfgang Paul in the 1950s [22] where radio-frequency (RF) electric fields are applied to generate a confining pseudo-potential.

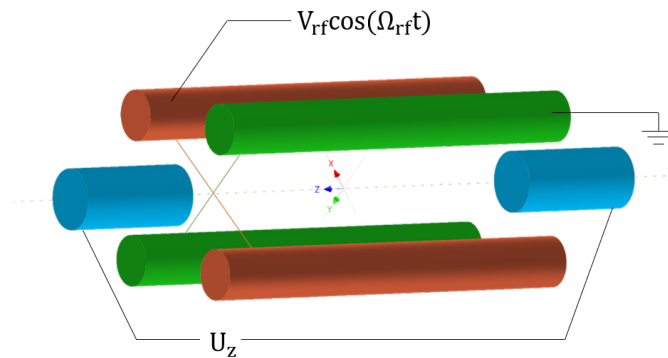


Figure 2.1: Schematics for a typical linear Paul trap (made with Autodesk Inventor). Four electrodes are arranged in a quadrupole configuration with two supplied $V_{rf} \cos(\Omega_{rf} t)$ (orange) and the other two grounded (green). Static potential U_z is applied to the endcaps (blue) for axial confinement.

In this type of ion trap shown in Figure 2.1, four electrodes in a quadrupole configuration are used for providing radial confinement, with an RF signal of amplitude V_{rf} and frequency Ω_{rf} applied to two of them and the other two grounded.

The resulting field potential at the trap center can be expressed as

$$\Phi = \Phi_0 + \kappa_{\text{rf}} V_{\text{rf}} \cos(\Omega_{\text{rf}} t) (x^2 - y^2), \quad (2.1)$$

where κ_{rf} is the geometrical factor of the RF electrodes. For axial confinement of the ions, static voltage U_z is applied to the endcaps which leads to a harmonic potential given as

$$\Phi_z = \kappa_{\text{ax}} U_z \left[z^2 - \frac{1}{2}(x^2 + y^2) \right], \quad (2.2)$$

where κ_{ax} is the geometrical factor for the endcaps.

The motion of an ion with mass M and charge e_0 in the field, $\{r_1(t), r_2(t), r_3(t)\} \equiv \{x, y, z\}$, can then be described by the Mathieu equations [23]

$$\ddot{r}_i + \frac{\Omega_i^2}{4} \left[a_i + 2q_i \cos(\Omega_{\text{rf}} t) \right] r_i = 0, \quad i \in \{1, 2, 3\} \equiv \{x, y, z\} \quad (2.3)$$

where parameters a_i representing the effect of DC components are given as

$$a_1 = a_2 = -\frac{1}{2} a_3 = -\frac{4e_0 \kappa_{\text{ax}} U_z}{M \Omega_{\text{rf}}^2} \quad (2.4)$$

and parameters q_i showing the effect of the RF field are given as

$$q_1 = -q_2 = \frac{4e_0 \kappa_{\text{rad}} V_{\text{rf}}}{M \Omega_{\text{rf}}^2}, \quad q_3 = 0. \quad (2.5)$$

In typical settings, we have $|a_i|, q_i^2 \ll 1$ and the solution of the ion motion can be approximated to the first order of q_i as

$$r_i(t) \approx r_i^{(1)} \cos(\omega_i t + \phi_i) \left[1 + \frac{q_i}{2} \cos(\Omega_{\text{rf}} t) \right], \quad (2.6)$$

where the phase ϕ_i and amplitude $r_i^{(1)}$ of the slow secular oscillation are given based on initial conditions. The frequency of this oscillation is given by

$$\omega_i \approx \frac{1}{2} \Omega_{\text{rf}} \sqrt{a_i + \frac{1}{2} q_i^2} \quad (a_i + q_i^2/2 > 0). \quad (2.7)$$

Therefore, the ion can be considered as a 3D harmonic oscillator with the Hamiltonian given as

$$H = \sum_i \hbar \omega_i \left(\hat{a}_i^\dagger \hat{a}_i + \frac{1}{2} \right). \quad (2.8)$$

where $\hat{a}_i^\dagger (\hat{a}_i)$ is the creation(annihilation) operator for phonon mode in direction $i \in \{1, 2, 3\} \equiv \{x, y, z\}$.

In a real trap, due to imperfections in trap assembling, there will be RF component also along the z axis, i.e. $q_3 \neq 0$. Besides, as will be described in Section 3.2, additional electrodes can be introduced to provide an extra quadratic field that modifies Equation 2.4 and in turn varies the trapping frequencies for creating 2D ion crystals.

2.2 Ytterbium ion qubit

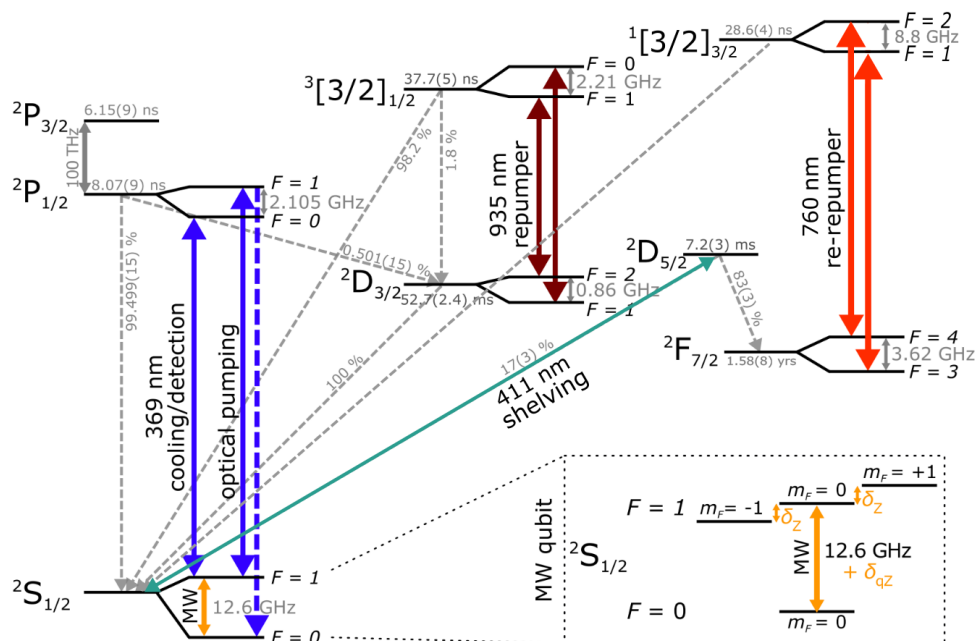


Figure 2.2: Level scheme of $^{171}\text{Yb}^+$ ions adapted from [24], with the 411 nm transition added for $^2F_{7/2}$ state shelving and the 638 nm repumper transition replaced by the 760 nm one used in the experiment. Hyperfine splitting and lifetime of $^1[3/2]_{3/2}$ given by [25] and [26]. Lifetime of $^2F_{7/2}$ updated from [27].

The ion used in our experiment is Yb^+ , in particular its isotope $^{171}\text{Yb}^+$ with hyperfine qubit transition in the ground state. As shown in Figure 2.2, the $^2S_{1/2} - ^2P_{1/2}$ transition of the $^{171}\text{Yb}^+$ ions has a linewidth of 19.6 MHz and can be used for Doppler cooling the trapped ions. Whenever the ions move against a cooling beam red-detuned from the transition, they absorb photons due to Doppler effect and then emit photons in random directions. Statistically, the ions experience a momentum kick along the direction of the beam after this scattering event and can be cooled in the trap towards the Doppler limit ($\hbar\Gamma/2k_B \sim 0.47\text{mK}$) which typically corresponds to phonon numbers in the order of ten.

The Doppler cooling is done experimentally by using a 369 nm laser with both σ_{\pm} and π components that drives the transition between $|^2S_{1/2}, F = 1\rangle$ and $|^2P_{1/2}, F = 0\rangle$, and a 12.6 GHz microwave signal for pumping the ions in $|^2S_{1/2}, F = 0\rangle$ to $|^2S_{1/2}, F = 1\rangle$. From the $^2P_{1/2}$ state the ion can decay to the metastable state $^2D_{3/2}$, and to $^2F_{7/2}$ due to background gas collisions. Therefore, a 935 nm laser and a 760 nm laser are introduced respectively to pump the ions back into the cooling cycle. The details of the laser setups are presented in Section 3.4.

The $^2S_{1/2} - ^2P_{1/2}$ transition can also be used for state preparation of the ions into the qubit state $|\downarrow\rangle = |^2S_{1/2}, F = 0\rangle$. During this process, the microwave signal is switched off and the frequency of the laser is modulated at 2.1 GHz with an electric-optic modulator (EOM) for bridging the hyperfine splitting of $^2P_{1/2}$, which improves the pumping rate[28].

However, in this thesis, the experiments are done on $^{174}\text{Yb}^+$ ions which has no nuclear spin and therefore no hyperfine structure. This makes the isotope easier to deal with and well-suited for preliminary testing of the experimental setup, which is the prime goal of my project.

2.3 Spin-spin interaction

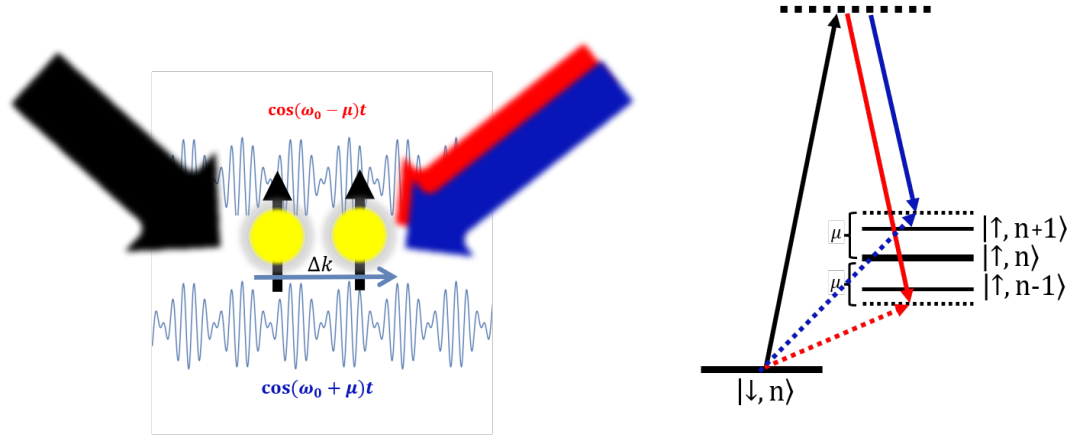


Figure 2.3: Schematics for the Raman laser setup that generates the spin-spin interaction following the Mølmer-Sørensen scheme. The red (blue) beam interferes with the black beam and form moving lattices with a beat frequency of $\omega_0 - \mu$ ($\omega_0 + \mu$), which corresponds to Raman red (blue) sideband coupling between the two qubit states with the detuning $\mu - \omega_m$ ($\mu + \omega_m$), where ω_m is the frequency of the relevant vibration mode. The momentum gain of the ions from this coupling is determined by the wave vector difference between the black beam and the red or blue beam Δk .

To generate Mølmer-Sørensen type of spin-spin interaction between the ion

qubits based on [19], we intend to utilize a Raman configuration using a high-power 368 nm laser as shown in Figure 2.3. Considering only the center of mass (COM) motion of the two ions along z direction with frequency ω_z , two sets of Raman transition with the opposite detuning $\pm\mu$ results in the Raman coupling on the two addressed ions in the form of

$$H = \hbar\eta_z\Omega(\sigma_+^1 + \sigma_+^2)(\hat{a}_m e^{i\delta t} + \hat{a}_m^\dagger e^{-i\delta t}) + H.c. \quad (2.9)$$

under rotating wave approximation, where $\sigma_+^{1,2}$ is the spin operator for ion 1 or ion 2 and $\delta = \mu - \omega_z$. $\eta_z = \Delta k_z z_0 \ll 1$ is the Lamb-Dicke parameter where $z_0 = \sqrt{\hbar/2M\omega_z}$ is the zero-point wavepacket size of a ion with mass M and Δk_z is the z component of $\Delta\mathbf{k}$, the wave vector difference between the black and the red or blue beam. The ions are assumed to be cooled within the Lamb-Dicke regime such that $\sqrt{\langle k_z^2 \rangle} \ll 1$ [12]. Ω is the Rabi frequency of carrier Raman coupling which is assumed to be the same for the two ions.

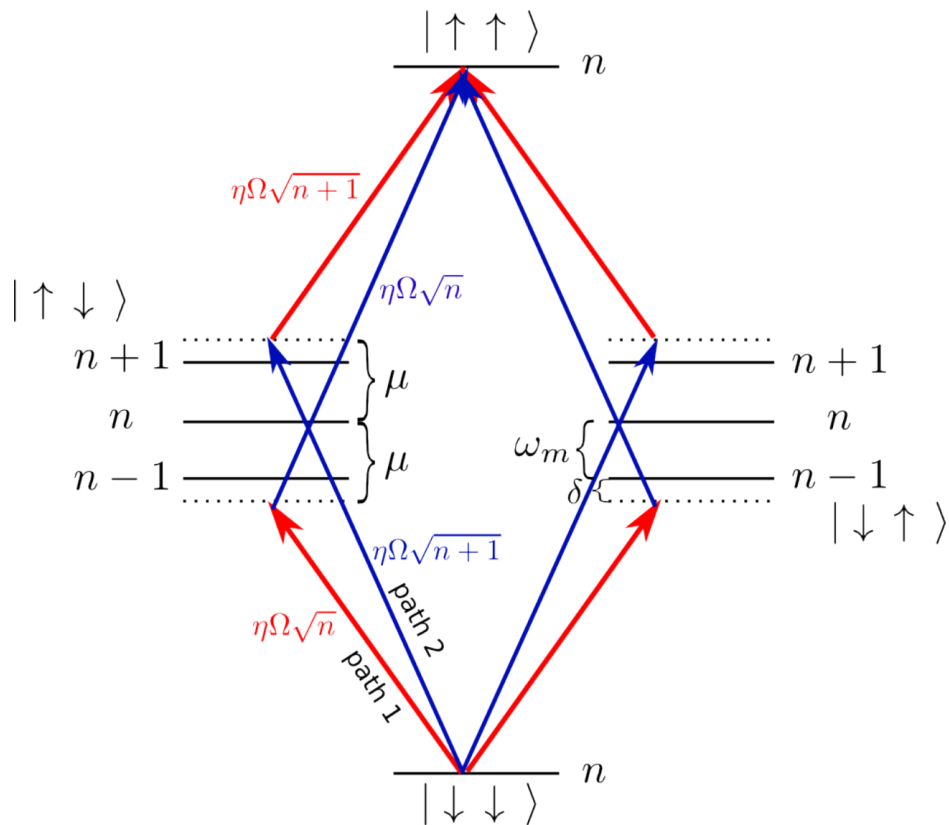


Figure 2.4: Mølmer-Sørensen scheme for generating spin-spin interaction in a 2-ion system, adapted from [29] where details for the calculation can be found.

With this Raman coupling, the state $|\downarrow\downarrow\rangle$ can be coupled to $|\uparrow\uparrow\rangle$ by one red sideband and one blue sideband transition as shown in Figure 2.4. When the detuning δ is larger than the sideband Rabi frequency $\eta_z\Omega\sqrt{n}$, where n is the phonon number, the coupling strength can be written based on perturbation theory as $(\eta_z\Omega)^2/(2\delta)$. The same coupling also presents between $|\downarrow\uparrow\rangle$ and $|\uparrow\downarrow\rangle$.

Considering also the coupling contributed by driving the red sideband transition with the blue beam and driving the blue sideband transition with the red beam¹, the coupling strength should also include $-(\eta_z\Omega)^2/(2\delta')$, where $\delta' = \mu + \omega_z$. Therefore, the spin-spin interaction generated can be expressed as

$$H_{\text{eff}} = \hbar J \sigma_x^1 \sigma_x^2 \quad (2.10)$$

where the interaction strength J is given by

$$\begin{aligned} J &= \frac{(\eta_z\Omega)^2}{2(\mu - \omega_z)} - \frac{(\eta_z\Omega)^2}{2(\mu + \omega_z)} \\ &= \frac{(\eta_z\Omega)^2\omega_z}{\mu^2 - \omega_z^2} \end{aligned} \quad (2.11)$$

In a more general case, the multiple phonon modes in an N-ion crystal should be considered (only the modes in z direction for simplicity). They can be calculated by diagonalizing the Hessian matrix \mathbf{A} from the Lagrangian describing the ion motion $q_i(t) = z_i(t) - z_i^0$ around its equilibrium position z_i^0 ($i = 1 \dots N$) in the crystal to the second order [30], given as

$$L = \frac{M}{2} \left[\sum_{i=1}^N \dot{q}_i^2 - \omega_z^2 \sum_{i,j=1}^N A_{ij} q_i q_j \right], \quad (2.12)$$

where ω_z is the trapping frequency along the z direction and the matrix elements $A_{ij} = [\partial^2 V / \partial z_i \partial z_j]_0 / M \omega_z^2$. Here V is the total potential energy of the ion crystal given by

$$V = \sum_{i=1}^N \frac{1}{2} M \omega_z^2 z_i(t)^2 + \sum_{i \neq j}^N \frac{e_0^2}{8\pi\epsilon_0} \frac{1}{|z_i(t) - z_j(t)|} \quad (2.13)$$

where ϵ_0 is the permittivity of free space. The frequency of the m^{th} phonon mode can thus be calculated as $\omega_m = \sqrt{\lambda_m} \omega_z$, where λ_m is the corresponding eigenvalue of the matrix \mathbf{A} . A more general form of the interaction strength between ion i and ion j is thus given in [19] as

$$J_{i,j} = (\eta_z\Omega)^2 \sum_m \frac{b_{i,m} b_{j,m}}{\mu^2 - \omega_m^2} \quad (2.14)$$

¹The counter-rotating term ignored by Equation 2.9.

where $b_{i,m}$ is the normalized mode vector components of ion i for mode m and $\sum_i |b_{i,m}|^2 = \sum_j |b_{j,m}|^2 = 1$.

By applying optical tweezers on the ions, both the normalized mode vector \mathbf{b}_m and mode frequency ω_m can be tuned such that intriguing spin-spin interaction patterns can be generated for simulating relevant spin systems [20], for example triangular, hexagonal and kagome spin lattices with frustration [31–33].

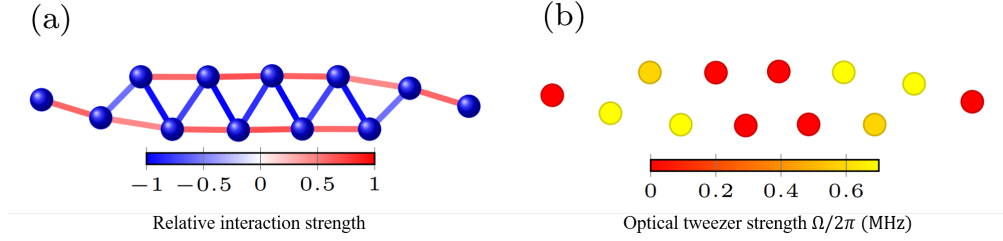


Figure 2.5: An example for tweezer-engineered spin-spin interaction simulating the spin frustration in spin-ladders where (b) shows the applied tweezer strength on the ions and (a) shows the consequent spin-spin interaction pattern. Adapted from [20] where more information can be found.

Chapter 3

Experimental Setup

In this chapter, the experimental setup that has been built will be described. Section 3.1 will be an overview of the vacuum system. In Section 3.2, the configuration of our ion trap and its electrode connection will be discussed. In Section 3.3, the photoionization process that generates Yb^+ ions and the homebuilt 399 nm laser system for it will be described. The current implementation of the lasers related to Doppler cooling the ions will be presented in Section 3.4. In the end, our imaging system and preliminary optical tweezers setup will be introduced in Section 3.5.

3.1 Vacuum system

As shown in Figure 3.1, the ion trap is placed inside a vacuum chamber with 8 viewports for optical access and electrical feedthroughs for trap electrodes connection and Yb oven connection. For reducing destructive background gas collisions with the ion crystals, ultra-high vacuum is sustained inside the chamber by an SEAS Z300 ion getter pump installed on the bottom left flange. The advantage of this pump is the intergration of an extra Non Evaporable Getter (NEG) pump for efficient pumping of H_2 , the main source of interactive collisions. The chamber was baked at 240°C with external turbo pump connected inside a large oven (Figure 3.2) following the baking procedure described in Figure 3.3.

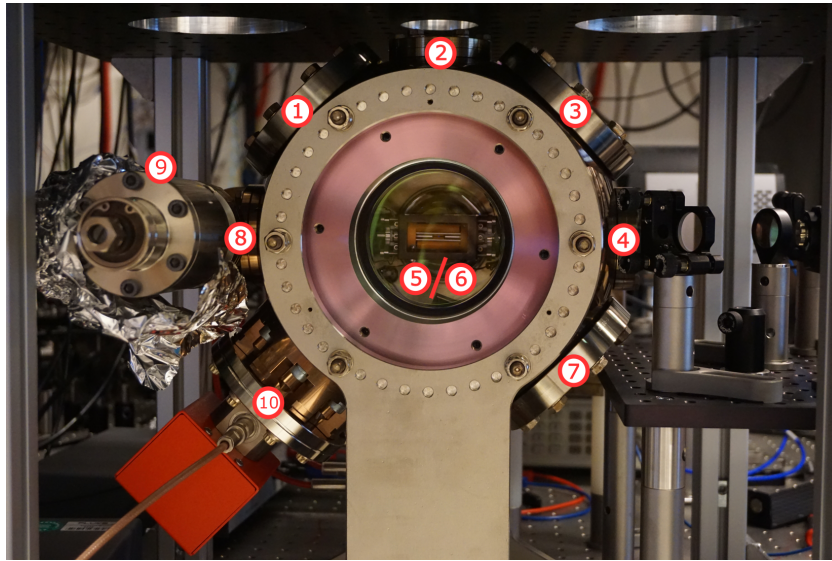


Figure 3.1: View of the experimental chamber from the imaging viewport. (① - ⑧) : viewports; ⑨ : connection to turbo pump; ⑩ : SEAS Z300 pump)



Figure 3.2: Picture of the vacuum chamber inside the oven for baking. The chamber is twined around with heat bands and wrapped with aluminium foil. A few thermocouples are mounted close to the chamber or inside the oven to monitor the temperature.

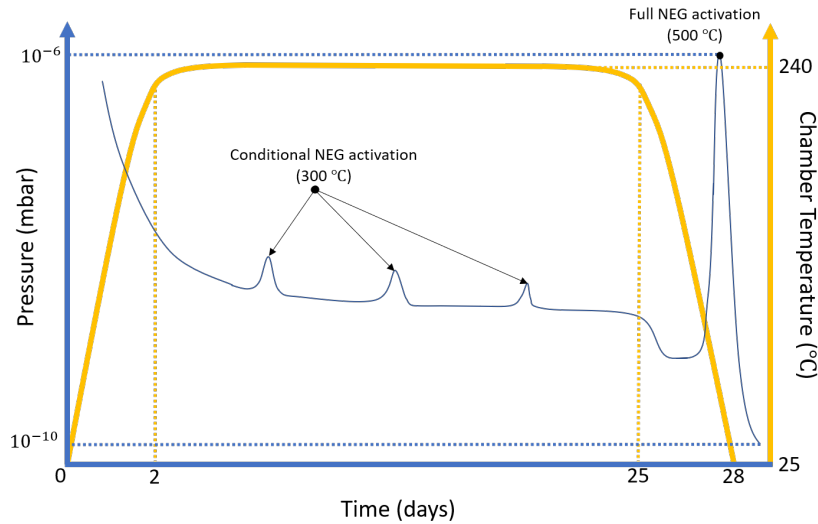


Figure 3.3: Schematics for the change in pressure and temperature of the chamber during the baking process. After ramping the temperature to 240 °C, several conditional activations of the NEG element are done by heating it to 300 °C, in order to release the particles it captured. After baking at 240 °C for around 3 weeks, the temperature is ramped down to room temperature again and a full activation of the NEG element is carried out by heating it to 500 °C. This helps to reduce the final pressure to below 10^{-10} mbar.

3.2 Ion Trap

3.2.1 Trap configuration

The ion trap used in our setup is a linear Paul trap with two pairs RF blades wirecutted from a single block of titanium and gold-plated. Before gold plating, the blades are etched with HF to smooth the surface and to remove titanium oxide (TiO₂) layer. This also permits better adhesion of the gold layer to the titanium substrate. The thickness of the gold layer that helps to conduct the RF signal is around 30 μm considering the skin depth at the desired RF frequency¹.

As shown in Figure 3.4b, the four blades are extended from two bases in pairs with two of them supplied RF power and the other two grounded to provide the radial confinement of the ions. The axial confining field is generated by applying the DC voltage on two end-caps mounted through the bases.

Around the RF blades are four pairs of DC electrodes. On the two pairs along the imaging plane, negative high voltages are applied for stretching the ion crystal from a 1D chain to a 2D plane. The other two pairs perpendicular to the imaging plane are further away from the ions and are used for micromotion compensation.

¹31.3 μm at 5.8 MHz.

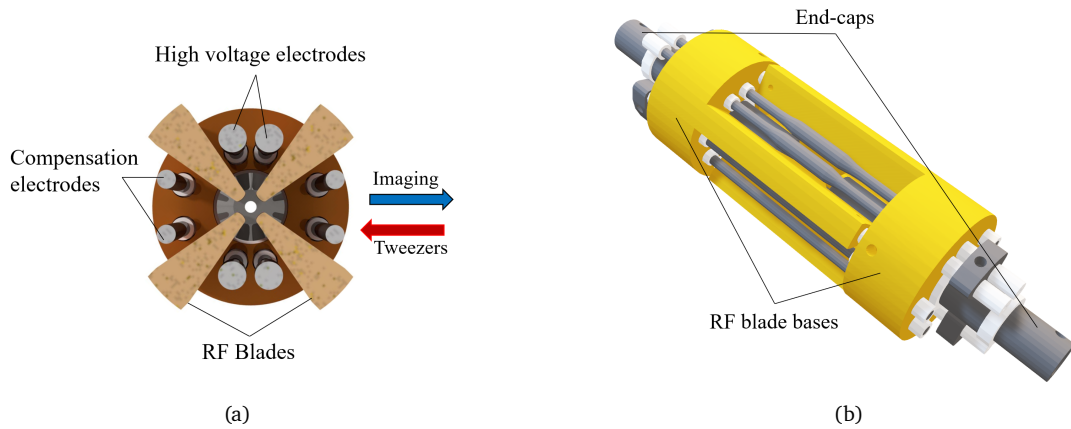


Figure 3.4: (a) Transverse section of the ion trap, showing the electrodes supplying static and RF electric fields for trapping 2D ion crystals and micromotion compensation. (b) Oblique view of the ion trap showing the full assembly.

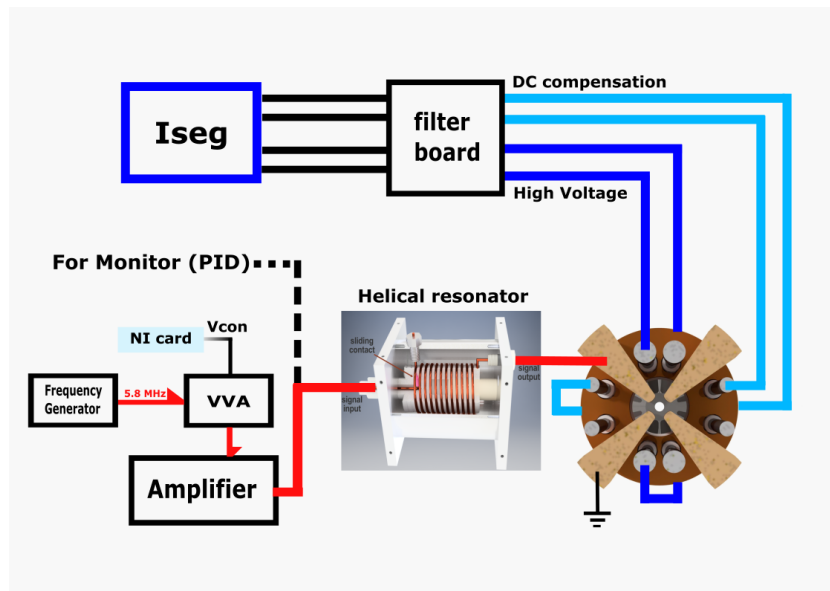


Figure 3.5: Electronic connection of the ion trap.

3.2.2 Electrode connection

As shown in Figure 3.5, the RF field for generating radially confining pseudo-potential is supplied by a home-built helical resonator² which filters and amplifies the signal from a signal generator³. To search for the resonance of the helical

²Manufactured by Electronics workshop, Technology Centre, University of Amsterdam.

³Hewlett-Packard 8657A, 0.1-1040 MHz

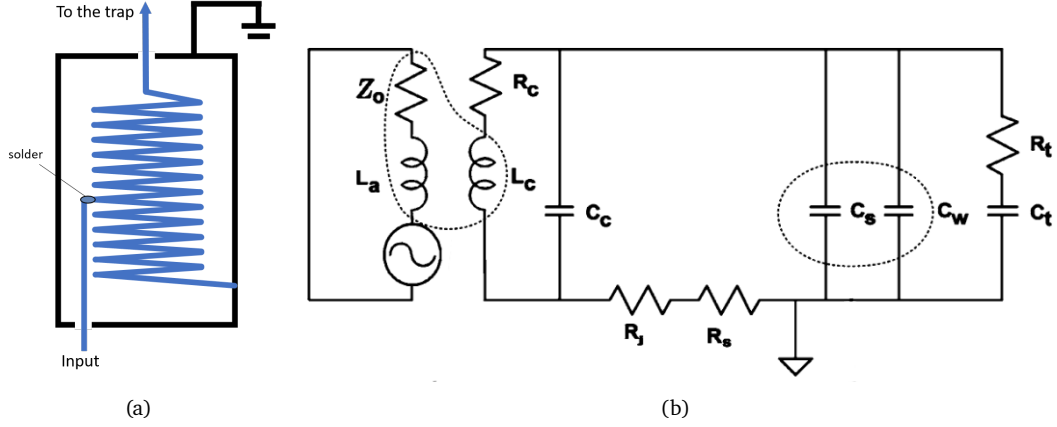


Figure 3.6: (a) Structure of the helical resonator. The coil (blue) is mounted on a plastic cylinder. It has 31 winding and is made of copper wire with a thickness of 0.8 mm. The shield is made of steel and silver-plated. The soldering point is chosen to achieve $Q \approx 3000$ with the resonance frequency around 6 MHz. (b) Diagram illustrating the electrical equivalent of the helical resonator circuits, adapted from [34]. Z_0 : RF source impedance; L_a : resonator antenna coil (input wire and the coil part between the soldering point and the grounding point) self inductance; L_c : resonator helical coil self inductance; R_c : resonator helical coil resistance; C_c : resonator helical coil self capacitance; R_j : helical coil to shield junction resistance; R_s : shield resistance; C_s : capacitance of helical coil to shield; C_w : capacitance of the wires connecting to ion trap; R_t : ion trap resistance; C_t : ion trap capacitance.

resonator, a directional coupler⁴ is used to pick up the reflected power from the helical resonator.

As shown in Figure 3.6b, the resonance frequency of the helical resonator can be estimated as

$$\omega_0 = \frac{1}{\sqrt{(C_s + C_t + C_w + C_c)L_c}}. \quad (3.1)$$

When input RF frequency approaches the resonance of the helical resonator, the power supplied to the RF blades increases and the capacitance of the ion trap C_t changes due to the thermal deformation of trap components, which leads to the shift in resonant frequency. Therefore, the frequency of the input RF signal needs to be adjusted continuously before the trap reaches thermal equilibrium. As shown in Figure 3.5, the radial confinement can be changed by a voltage variable attenuator (VVA) controlled by a National Instrument (NI) analog output device⁵. However, this leads to a change in RF power and in turn breaks the thermal equilibrium. Therefore, the frequency adjustment needs to be redone after every tuning.

⁴Mini-Circuits ZDC-10-1+.

⁵National Instrument NI6738.

The DC high voltages on the electrodes are supplied by an Iseg module⁶. It contains two individual DC power supplies, one with 12 analog output channels ranging from -1.5 kV and 1.5 kV and the other with 4 negative high voltage output up to -10 kV. The 12-channel module output has a ripple of less than 20 mV while the ripple of 4-channel high voltage module output is 3 mV (> 1 kHz) and 10 mV (10 Hz - 1 kHz), which ensures stable trapping potential. The maximum voltage ramping speed of the modules can be $1 \cdot V_{\max}/s$ for the 12-channel one and $0.2 \cdot V_{\max}/s$ for the 4-channel high voltage one, which makes possible the rapid transition from 1D to 2D crystal configuration in the experiment.

3.3 Photoionization

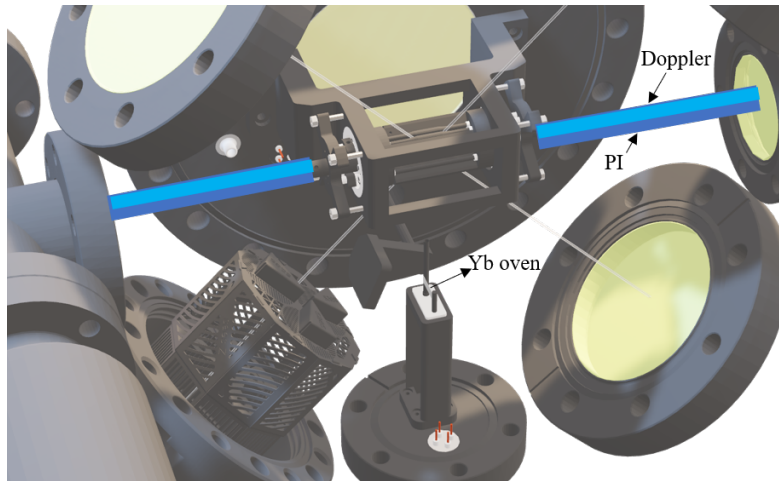


Figure 3.7: Configurations of the laser beams used for photoionization at the trap. Below the trap, an Yb oven is mounted on a flange which consists of two stainless steel rods connected to a tantalum plate. One of the rods is hollow and filled with Yb. It generates Yb atom flux when heated up by supplying current through the tantalum plate. At the trap center, these atoms are photoionized and cooled by the 399 nm Photoionization (PI) laser and the 369 nm Doppler cooling laser based on a two-stage photoionization process as described in the text.

⁶Iseg CC24, EBS C0 30, and EHS 40 100n in ECH42 rack system.

As shown in Figure 3.7, an Yb oven below the trap is used to produce the Yb atoms used in the experiment when driven with current⁷. The atoms are in turn photoionized into ions and confined in the trap. Following the scheme shown on the right, a 399 nm photoionization (PI) laser is introduced to excite the Yb atoms near the trap center to 1P_1 state, where the absorption of the 369 nm Doppler cooling light is sufficient to remove one electron from the outer shell of the atoms. This two-stage photoionization process leads to controllable loading of Yb^+ ions into the trap in the sense that the ion loading rate can be tuned by changing the driving current of the Yb oven and the intensity of the PI laser beam. Whereas the saturation intensity of the $^1S_0 - ^1P_1$ transition $I_{sat} = 60 \text{ mW/cm}^2$, an intensity of $\gtrsim 400 \text{ mW/cm}^2$ for the 399 nm laser beam is used in the experiment to achieve decent loading rate (about 5 ions/min). In addition, by changing the frequency of PI laser, the type of ionized Yb isotope can also be chosen given the isotope dependence of the $^1S_0 - ^1P_1$ resonance frequency [36].

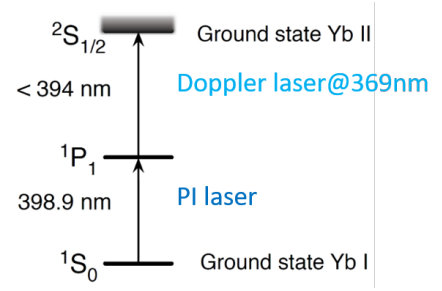


Figure 3.8: Two-stage photoionization process for Yb, adapted from [35].

Homebuilt 399 nm laser

To trigger the first stage of the photoionization procedure, an external cavity diode laser (ECDL) system operating at 399 nm has been built. The system is adapted from an 480 nm laser that was not longer used [37], with the laser diode (LD) replaced by Nichia NDV4316.

As in a typical Littrow configuration, a single optical mode is selected to lase from the free running spectrum of the LD based on holographic grating based feedback. The collimated beam from the LD is diffracted by the grating and the 1st order diffracted light couples back into the LD at the wavelength $\lambda = 2d \sin \theta$. Here, d is the grating constant and the diffraction angle θ can be tuned by rotating the grating. For convenience, we kept the grating⁸ used for 480 nm laser with $d = 2400 \text{ lines/mm}$ and the targeting diffraction angle for 399 nm can be calculated to be 28.7° . In this feedback mechanism, the grating serves as an outcoupler of an external cavity that further narrows down the linewidth of the transmitted mode. Given the sensitivity of the external cavity and the LD to temperature, both the temperature of the LD itself and the whole block are stabilized via Peltier modules controlled by home-built electronics. A current controller was also built for the

⁷Operating at 3.7 A in the experiment.

⁸Thorlabs GH13-24U, UV Reflective Holographic Grating.

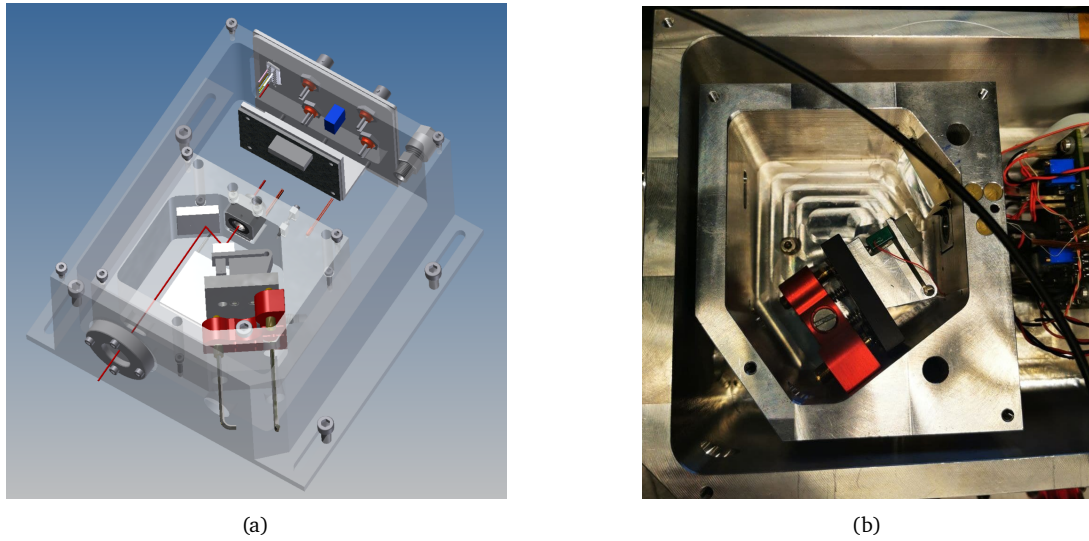


Figure 3.9: (a) Design of the homebuilt 399 nm external cavity diode laser, adapted from [37]. The beam path inside the laser is shown in red line. (b) Photos of the 399 nm laser's internal structure.

system to provide stable control over the driving current of the LD. The electronics are designed in [38] and the circuit diagrams are shown in Appendix A.

To align this external cavity generated from diffraction, an aspherical lens⁹ is mounted in front of the diode with its position carefully tuned to collimate the beam. The LD is rotated such that the long axis of the collimated elliptical beam is aligned horizontally and the polarization of the beam becomes vertical. Since the mounted grating has its lines along the vertical direction, the diffraction efficiency is lower for vertically polarized incident light and more output power from the laser can be obtained. By changing the laser polarization from horizontal to vertical, we managed to increase the output laser power by 60%. With proper alignment, single mode operation at the target wavelength is realized at a temperature of 26.1 °C and driving current of 55 mA. Measurement of the output power versus driving current is shown in Figure 3.11 which indicates the threshold current to be around 44 mA.

⁹Thorlabs C230TMD-A, $f=4.51$ mm, $NA=0.55$, AR-coated: 350-700 nm.

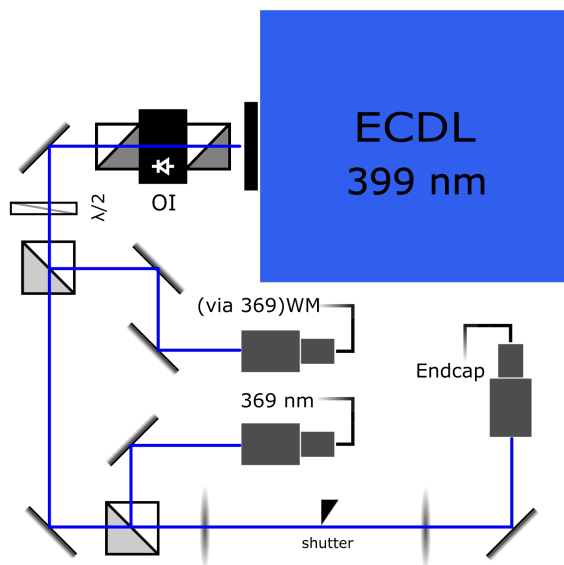


Figure 3.10: The optical setup for the 399 nm laser. A LINUS FI-405-5SV optical isolator (OI) is placed right after the laser to prevent retro-reflected light from going back to the LD and thus improves the lasing mode stability. Part of the laser power is sent to our HighFinesse WS7-30 wavemeter for monitoring the wavelength. The main branch of the laser is combined with the 369 nm light and sent through the endcaps.

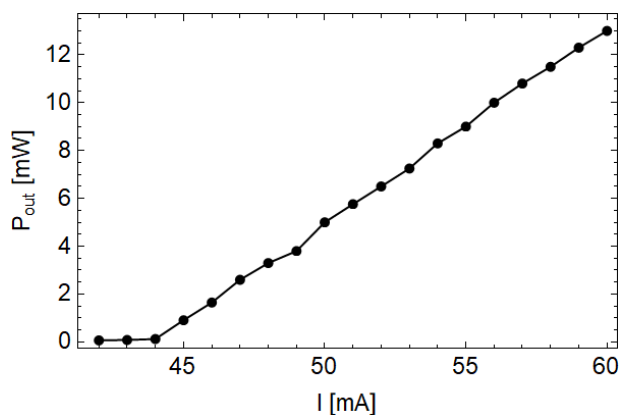


Figure 3.11: Output power from the PI laser after optical isolator at different driving currents.

3.4 Laser configuration

Besides the 399 nm laser, several laser setups have been implemented for laser cooling the Yb^+ ions, including $^{174}\text{Yb}^+$ for preliminary experiments and $^{171}\text{Yb}^+$ for future quantum simulation and quantum information processing experiments. As shown in Figure 3.12, the ions are Doppler cooled on the transition between

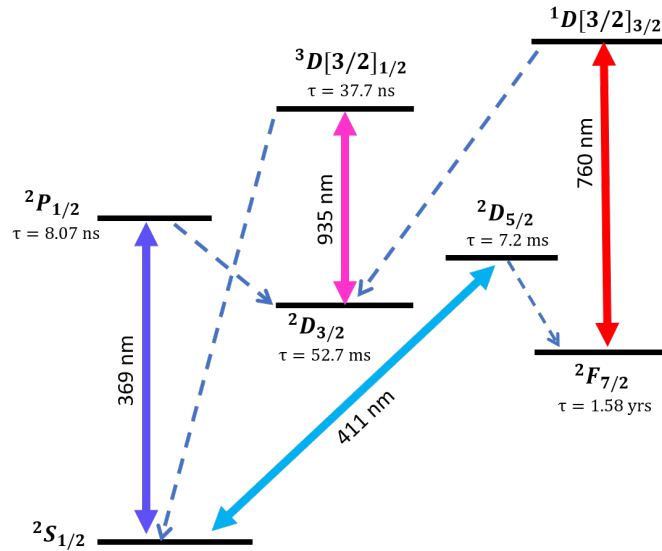


Figure 3.12: Level scheme for the Ytterbium ion.

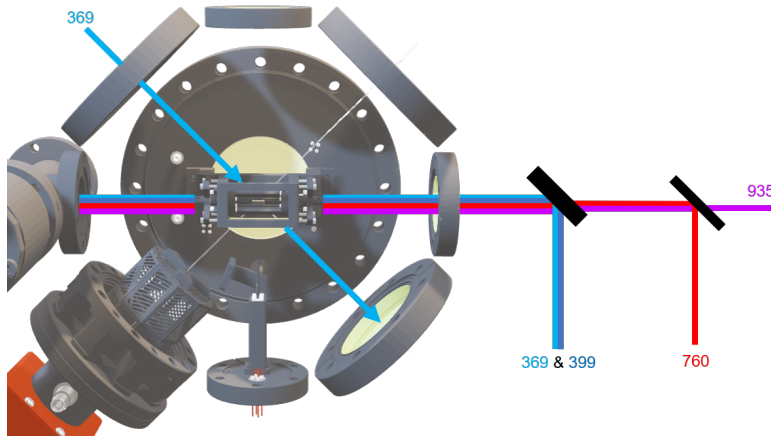


Figure 3.13: Laser configuration around the trap. The beams sent through the endcap contains 399 nm light for photoionization, 369 nm for preliminary Doppler cooling, and 760 nm and 935 nm for repumping. The prime Doppler cooling beam is applied from the top left flange to achieve efficient cooling in all directions.

$^2S_{1/2}$ and $^2P_{1/2}$. Since ions can decay to the metastable state $^2D_{3/2}$ and to the $^2F_{7/2}$ state via background gas collisions during Doppler cooling, repumper lasers are required for pumping them back to the cooling cycle. These cooling and repumper lasers are sent through the endcaps along with the PI laser such that they are well aligned to the ion crystal, as illustrated in Figure 3.13. An additional Doppler laser beam is applied from the top left viewport for more efficient cooling and imaging,

since the endcap cooling beam along the axis is far red-detuned and is inefficient for cooling the radial motion of the ions.

3.4.1 369 nm Doppler setup

The 369 nm transition is driven by a DL Pro diode laser from Toptica with the optical setup shown in Figure 3.14. As mentioned above, two branches of the setup are involved in Doppler cooling the ions. The Doppler beam through the endcap has a typical power of $300 \mu\text{W}$ at the frequency of the laser, which is far red-detuned by 170 MHz from the transition to enhance loading. The frequency of the prime cooling beam from the top instead is detuned only by -10 MHz, shifted by an acoustic-optic modulator¹⁰ (AOM) operating at 160 MHz. The power of this beam can also be changed by varying the driving power of the AOM and the maximum power is measured to be around $140 \mu\text{W}$. This branch also contains an electro-optic modulator¹¹ (EOM) that can be used to generate the 2.1 GHz sideband for optical pumping $^{171}\text{Yb}^+$ ions to $F = 0$ qubit state in the future.

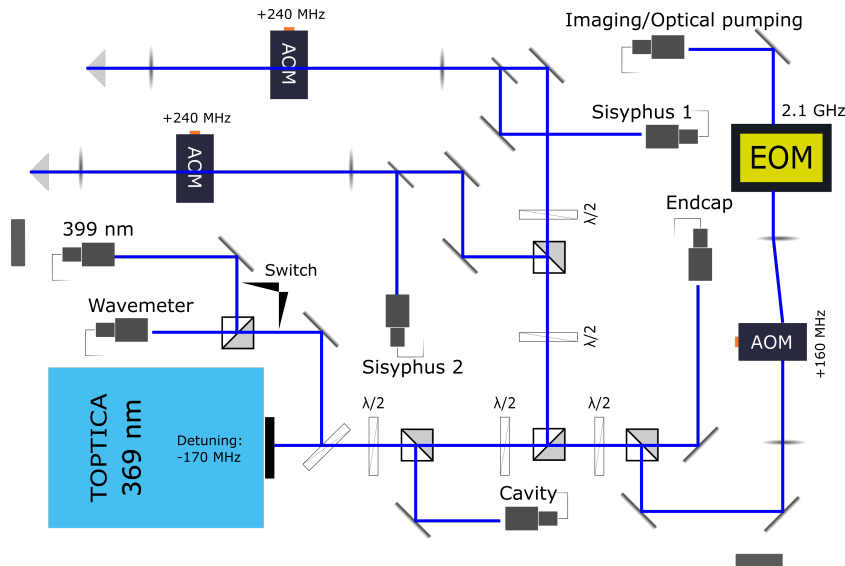


Figure 3.14: Layout for the 369 nm laser setup with the details described in the text.

In the configuration, another two AOMs of the same type is operating at 240 MHz in the double-pass manner. They can be used to generate a pair of counter-propagating beams detuned by $+310$ MHz for implementing the Sisyphus cooling scheme [39], which helps to cool the ion crystal further into the Lamb-Dicke regime. The beams will create polarization gradient lattices at the trap center,

¹⁰Gooch & Housego 3200-1210.

¹¹QUBIG PM-Yb+ _2.1.

where the ions experience state dependent periodic potential. Whenever they roll up the potential "hills" they are pumped to lower state and lose kinetic energy. In this way, a lower temperature of the crystal can be obtained exceeding the Doppler cooling limit. One alternative way of achieving this is the electromagnetically-induced-transparency cooling method investigated recently in [40, 41].

3.4.2 935 nm Repumper setup

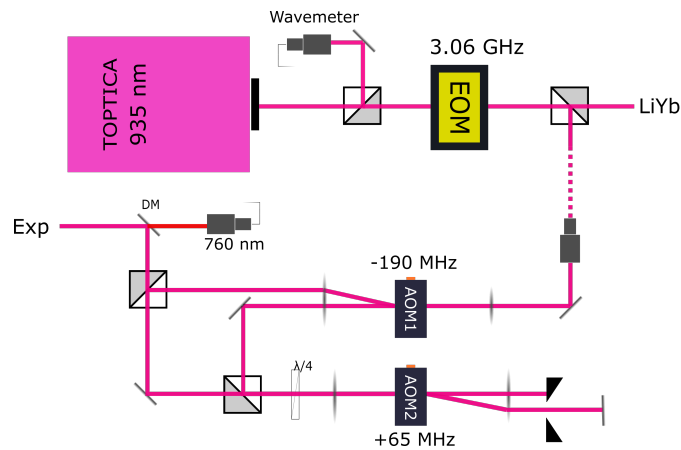


Figure 3.15: Layout for the 935 nm laser setup with the details described in the text. EOM: QUBIG E0-T3070-3M; AOM1: Gooch & Housego 3200-124; AOM2: ISOMET 1205C.

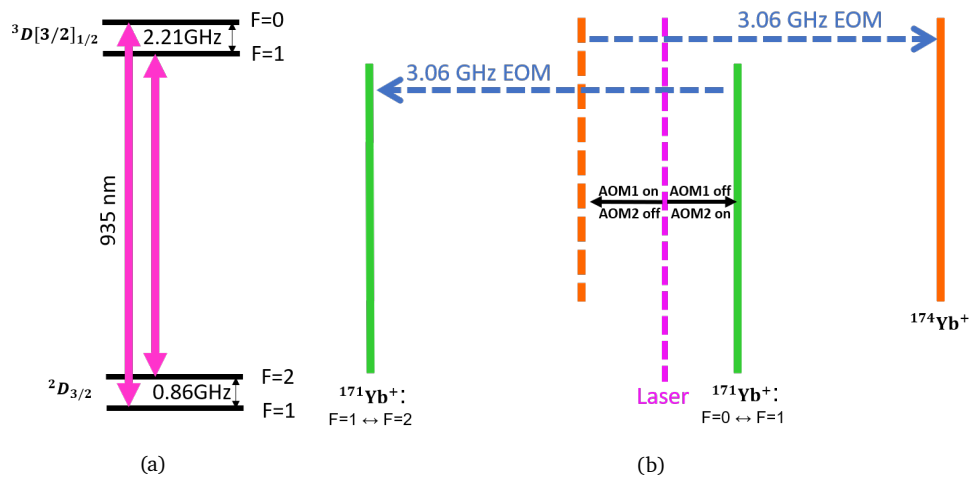


Figure 3.16: (a) 935 nm repumper transition for $^{171}\text{Yb}^+$. (b) Schematics for the isotope switch of the 935 nm laser setup.

The 935 nm laser for repumping the ions back from $^2D_{3/2}$ state is another Toptica DL Pro diode laser, with the setup shown in Figure 3.15. For $^{171}\text{Yb}^+$, an EOM is used in the setup to bridge the 3.06 GHz hyperfine splitting of the repumper transition. As illustrated in Figure 3.16, two AOMs are implemented for switching between the resonance frequency of $^{174}\text{Yb}^+$ and $^{171}\text{Yb}^+$ while keeping the frequency of the laser unchanged since it is shared between two experiments. With AOM1 on and AOM2 off, only the -1 order of AOM1 will be sent to the experiment, the blue sideband generated by the EOM will thus be resonant with the $^{174}\text{Yb}^+$ transition. Otherwise, with AOM1 switching off but AOM2 on, the 935 beam will contain only the +1 order of AOM2 which is shifted to the resonances of $^{171}\text{Yb}^+$.

3.4.3 760 nm Repumper setup

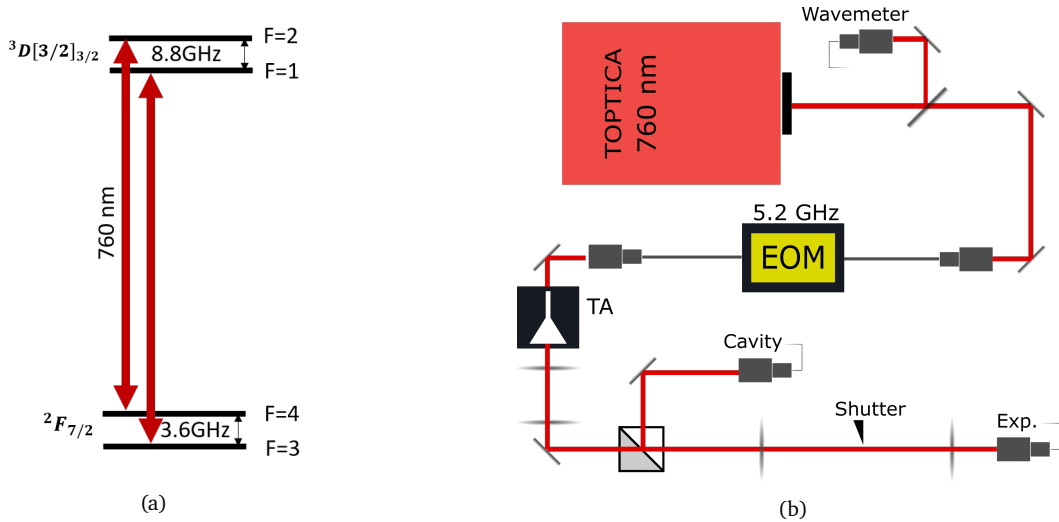


Figure 3.17: (a) 760 nm repumper transition for $^{171}\text{Yb}^+$. (b) Layout for the 760 nm laser setup.

The 760 nm laser is also a Toptica DL Pro laser which is used for pumping the ions back to the cooling transition when they decay from $^2P_{1/2}$ or $^2D_{3/2}$ state to the $^2F_{7/2}$ state due to background gas collisions. It will also be shared between two experiments so a homebuilt tapered amplifier¹² (TA) is implemented to amplify the power up to 800 mW when supplied with 2.3 A current at 20 °C. For now, one main branch has been built for our experiment and part of the laser power is sent to an optical cavity (see Section 4.1.2) for frequency stabilizing it.

¹²Based on Eagleyard EYP-TPA-0765-01500-3006-CMT03-0000 as described in [42].

3.5 Imaging and optical tweezers

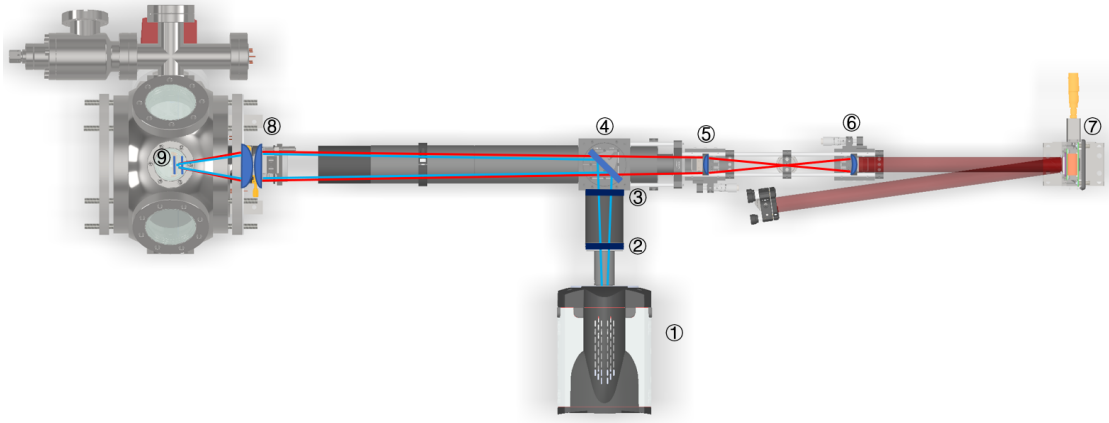


Figure 3.18: Schematics for the imaging system and the optical tweezers setup. ①: Andor iXon Ultra 897 EMCCD camera; ②: Semrock FF01-370/6-25 bandpass filter; ③: back polished mirror for 780 nm; ④: Thorlabs DMLP505L dichroic mirror; ⑤: Thorlabs LE1234-B lens; ⑥: Thorlabs LBF254-150; ⑦: LCOS-SLM X10468, Hamamatsu spatial light modulator; ⑧: lens doublet of AFL50-80 from Asphericon and LA4745 from Thorlabs, both coated for 369 nm and 805 nm; ⑨: ions in the trap.

As shown in Figure 3.18, the imaging of the trapped ions is done by probing the scattered 369 nm photons with an electron-multiplying charge-coupled device (EMCCD) camera (①). The active area of the camera sensor is a 512×512 array of pixels with the size of $16 \times 16 \mu\text{m}^2$. The pixels have about 30% quantum efficiency for detecting 369 nm photons and the maximum pixel readout rate of the camera is 17 MHz. With the frame transfer technique [43] that uses part of the pixels as buffers, the frame rate of the camera can reach 11074 fps. Therefore, besides real-time monitoring of the ions, the camera can also be used for state detection of the $^{171}\text{Yb}^+$ ion crystal in the experimental sequences. Since the camera can be externally triggered with our FPGA, the detection can be synchronized with the imaging 369 nm laser pulse generated by the corresponding AOM (see Section 4.1.1).

The 369 nm light from the ions are imaged onto the camera using a lens doublet (⑧) optimized for aberration with $\text{NA} = 0.29$. Before the camera, a bandpass filter (②) is installed to filter all the other laser light in experiment reflected by the trap.

The optical tweezer setup is coupled into the imaging system using a dichroic mirror (④). The optical tweezers are generated by shining collimated 805 nm light on a spacial light modulator (SLM) shown in (⑦). The light is from a tapered

amplifier laser system¹³ described in [24]. The system can produce up to 2W laser power with a tunable wavelength between 795 and 810 nm. Therefore, an extra back-polished mirror is placed between the camera and the dichroic mirror to further reduce background counting brought by the tweezer light on the camera.

At the SLM, the liquid crystal array of the SLM introduces an extra phase $\phi(x, y)$ to the incident light field. The target optical tweezer pattern can then be generated after Fourier transformation at the focal plane of the subsequent lens ((6)). The optical tweezers are applied to the ions in the trap center through the optical system consisting of an extra lens ((5)) and the imaging lens doublet which provides demagnification of around 8. For a given optical tweezer pattern, the required phase pattern on the SLM is calculated using the Iterative Fourier Transform Algorithm (IFTA) as is further discussed in [44].

¹³Toptica TA Pro

Chapter 4

System Control

In this chapter, the systems for the experimental control built during the project will be described. For controlling the lasers, Section 4.1 describes the homebuilt AOM driver that realizes AOM-based laser power control, and emphasizes the frequency stabilization system of the lasers including the locking of the 760 nm laser on a homebuilt cavity and the locking of the 369 nm and the 399 nm laser on the wavemeter. Besides laser controls, Section 4.2 presents the programming of the Iseg module control on our master control program (MCP) for controlling the voltage on the trap electrodes to generate 2D ion crystals. A brief introduction to the MCP itself is also given in this section.

4.1 Laser control

4.1.1 Power control based on AOM

Acoustic-optic modulators are widely used in the laser setups introduced in the last chapter. Such a device utilizes the RF wave traveling through its internal crystal as an effective optical grating that diffracts the incident beam. Following the Bragg diffraction process shown in Figure 4.1, the change in momentum during the photon scattering reflects also the shift in energy or frequency. For instance, the frequency of the +1 order diffraction beam is shifted blue from the fundamental beam by a unit of the RF frequency applied to the AOM and the frequency of the -1 order diffraction beam is shifted red by the same amount.

This mechanism makes it possible to tune the power of the diffracted beam by changing the RF driving power of AOM. This is done in our experiment via homebuilt AOM driving modules with the design illustrated in Figure 4.2. A voltage-controlled oscillator¹ (VCO) is used to generate the original RF signal

¹Mini-Circuits ZX95-310A-S+ (200 MHz AOMs); Mini-Circuits ZX95-100+ (80 MHz AOMs).

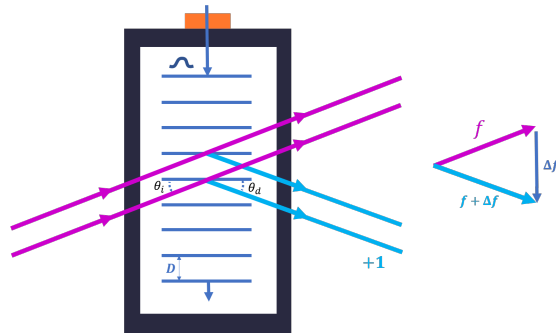


Figure 4.1: Schematics for the mechanism of acoustic-optic modulator.

at the required frequency and the power of the signal is controlled by a voltage-variable attenuator² (VVA) based on the control voltage V_{con} . The signal can also be switched on and off within tens of nanoseconds using an RF switch³ to generate laser pulse sequences. Finally, an amplifier⁴ is used to amplify the power of the signal for maximizing the diffraction efficiency of the AOM.

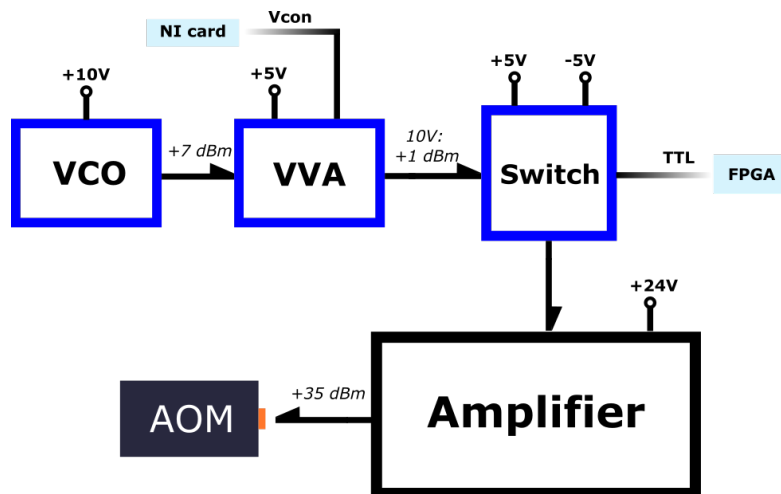


Figure 4.2: Driving circuits for AOM based on voltage-controlled oscillators (VCO), voltage-variable attenuators (VVA), RF switches and RF amplifiers from Mini Circuits. The details are described in the text.

²Mini-Circuits ZX73-2500+.

³Mini-Circuits ZYSW-2-50DR+.

⁴Mini-Circuits ZHL-1-2W+.

4.1.2 Frequency Locking on cavity

The frequency of the 760 nm laser is stabilized to a homebuilt Fabry-Perot cavity adapted from the one built in [24]. As shown in Figure 4.3, the laser is sent into the cavity with the transmitted light monitored by a CCD camera and the reflected power probed by a photodiode (PD). Based on the frequency dependence of the reflected laser power from the cavity, Pound-Drever-Hall (PDH) type of locking is realized based on a lock-in amplifier built upon a portable FPGA device⁵ and the Topica digital laser controller⁶ with its built-in PID feedback module.

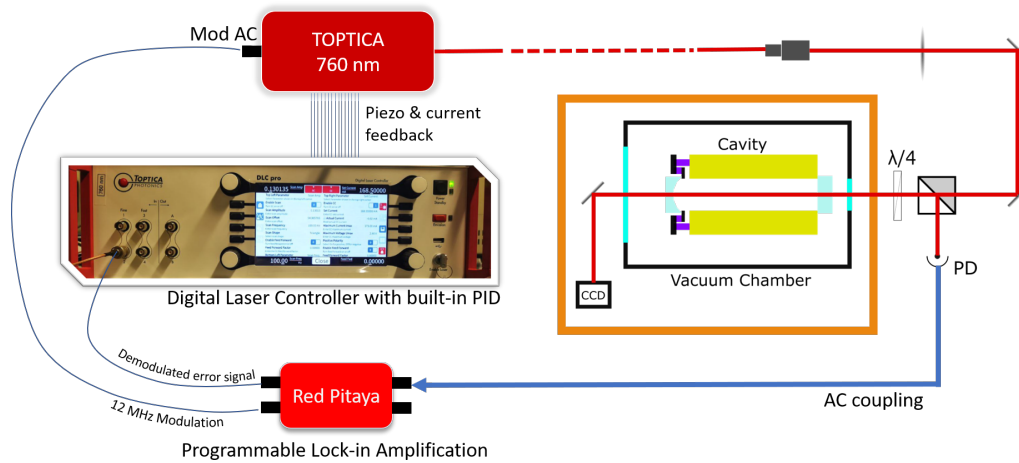


Figure 4.3: Schematics for the cavity locking system.

Homebuilt Fabry-Perot cavity

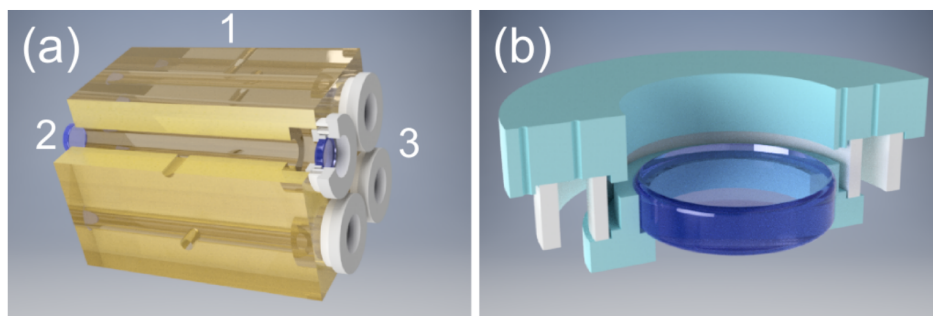


Figure 4.4: 3-D drawings of the reference cavity, adapted from [28].

⁵Red Pitaya STEMLab 125-14

⁶Topica DLC pro

The cavity used in this locking scheme is one of the four ports of an optical reference cavity system based on a Zerodur[®] glass block⁷ with an ultra-low thermal expansion coefficient. As shown in Figure 4.4, a cavity unit is built by mounting two cavity mirrors⁸ on both sides of a tunnel through the Zerodur block. The length of the block is 100 mm and the free spectral range of the cavities can be calculated to be 1.5 GHz. One of the cavity mirrors is mounted on a macor base⁹ that contains two piezoelectric rings¹⁰ for tuning the cavity length and in turn the resonance of the cavity. By using two piezoelectric rings instead of one, the thermal expansion of the rings will have negligible influence on the cavity length [28]. The parts are cleaned in ultrasonic bath using demineralised water and isopropanol and glued together with UV-curing epoxy¹¹. After placing the block inside a vacuum chamber, the chamber is baked at 95 °C for three days and the pressure is pumped down to around 10⁻⁸ mbar.

Pound-Drever-Hall scheme

As in a typical PDH configuration[45], the laser beam is well aligned to the axis of the cavity and the reflected signal from the (PD) can be used to indicate the frequency difference between the laser frequency and the resonance of the cavity. By scanning the laser frequency, a dip can be seen in the reflected signal with the intensity of the transmitted beam profile at its maximum when the light frequency matches one of the cavity longitudinal modes.

With laser frequency modulated at ω_m , the incident light field will contain sidebands as shown in:

$$\begin{aligned} E_i &= E_0 e^{i(\omega t + \beta \sin \omega_m t)} \approx E_0 e^{i\omega t} [1 + i\beta \sin \omega_m t] \\ &= E_0 e^{i\omega t} \left[1 + \frac{\beta}{2} e^{i\omega_m t} - \frac{\beta}{2} e^{-i\omega_m t} \right]. \end{aligned} \quad (4.1)$$

where β is the modulation strength, ω is the frequency of the laser and E_0 denotes the amplitude of the incident field. The modulation is done by modulating the current of the laser for its "Mod AC" connector with the modulation signal generated by the lock-in amplifier. In this way, the reflected light field will become:

⁷Custom made by SCHOTT AG, Expansion Class 0. Modified by Glass Instrumentation, Technology Center, University of Amsterdam.

⁸Altechna plano/plano HR mirror: UVFS, Φ 12.7 mm, thickness 5 mm, S1[R>99.7% @740-760nm(AOI=0°)], S2[R<0.25% @740-760nm(AOI=0°)]; Altechna plano-concave HR mirror: UVFS, Φ 12.7 mm, edge thickness 5 mm, ROC=-250 mm S1[R>99.5% @740-760nm(AOI=0°)], S2[R<0.25% @740-760nm(AOI=0°)].

⁹Manufactured by mechanical workshop, Technology Center, University of Amsterdam.

¹⁰MEGGITT A/S OD24.4 ID22.4 L4 and OD18.3 ID16.7 L4

¹¹Epoxy Technology, OG142-112

$$E_r = E_0 [R(\omega)e^{i\omega t} + R(\omega + \omega_m)e^{i(\omega+\omega_m)t} - R(\omega - \omega_m)e^{i(\omega-\omega_m)t}]. \quad (4.2)$$

Here, the frequency dependent reflection function

$$R(\omega) = \frac{E_r}{E_i} = \frac{(r_1^2 + t_1^2)r_2 e^{2\pi i\omega/\omega_0} - r_1}{1 - r_1 r_2 e^{2\pi i\omega/\omega_0}}, \quad (4.3)$$

where $r_{1,2}$ and $t_{1,2}$ are reflection and transmission coefficients of mirror 1 and mirror 2 of the cavity and ω_0 denotes the angular free spectral range of the cavity.

The reflected laser power can in turn be expressed as:

$$P_r = P_0 \left\{ |R(\omega)|^2 + \frac{\beta^2}{4} [|R(\omega + \omega_m)|^2 + |R(\omega - \omega_m)|^2] \right\} + P_0 \beta \{ \text{Re}[\chi(\omega)] \cos \omega_m t + \text{Im}[\chi(\omega)] \sin \omega_m t \} + P(2\omega_m) \quad (4.4)$$

where $\chi(\omega) = R(\omega)R^*(\omega + \omega_m) + R^*(\omega)R(\omega - \omega_m)$. The terms oscillating in ω_m are of particular interest since the coefficient $\chi(\omega)$ shown in Figure 4.5 is an asymmetric function indicating the frequency error $\Delta\omega = \omega - N\omega_0$. Encoded around the modulation frequency, the error signal is also protected from low frequency noise in the circuits that can be eliminated with a low-pass filter after mixing the reflection signal with the modulation signal for decoding.

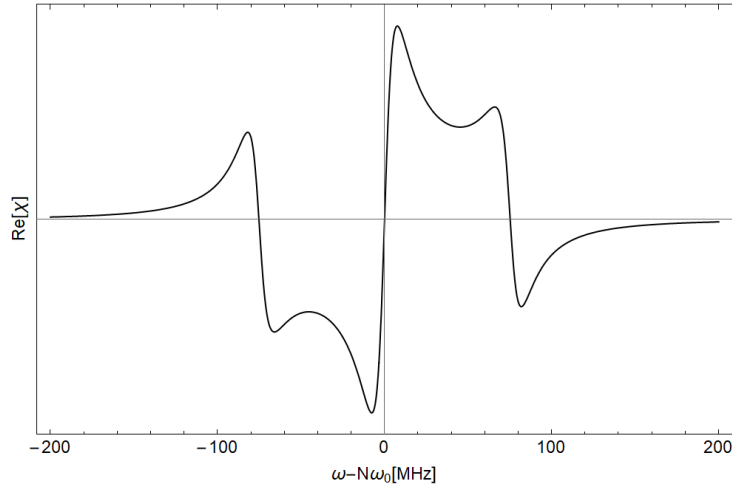


Figure 4.5: Plot of the $\text{Re}[\chi(\omega)]$ function.

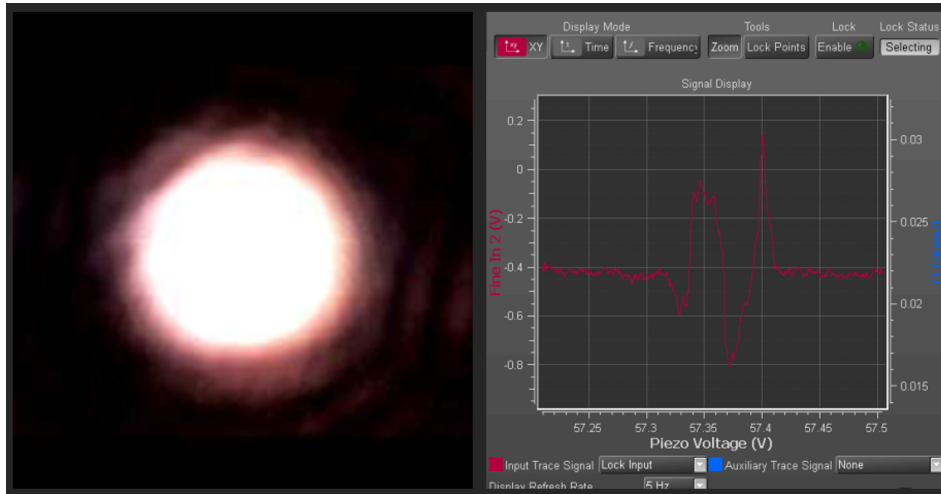


Figure 4.6: The cavity mode on CCD and the error signal after demodulation.

Lock-in amplification and PID feedback

As mentioned above, this modulation-demodulation procedure is done with a lock-in amplifier designed on a Red Pitaya device. Various measurement and control can be realized on this compact FPGA device, as is discussed in [46]. It has two input and two output channels which can be monitored and controlled via network connection from a graphic user interface (GUI) shown in Figure 4.7 generated by the PyRPL¹² package. The program can generate so-called IQ-modules which are programmed to calculate the output signal for the selected output channel from the input signal, based on the shown circuit diagram. The parameters in the circuit can be carefully chosen to realize target functions.

For lock-in amplification of the error signal, the "IN1" channel of the device is connected to the PD and shows the reflective power from the cavity. With properly set parameters, the device supplies modulation signal with frequency $\omega_{mod} = 12$ MHz to the laser current controller connected to its "OUT1" channel. The modulation signal also contains a tunable phase ϕ to compensate for the phase delay in the circuits. On "OUT2" channel, the demodulated input signal after parameter-controlled filters is generated.

The demodulated error signal is subsequently processed at the Toptica DLC Pro laser controller. It contains two built-in PID modules where "PID1" is used for high frequency feedback on laser driving current and "PID2" is used for relatively slow feedback on the piezoelectric transducer (PZT) voltage. Based on the PZT driver, the controller can also be used to tune and scan the laser frequency for searching the proper peak to lock.

¹²<https://pyrpl.readthedocs.io>

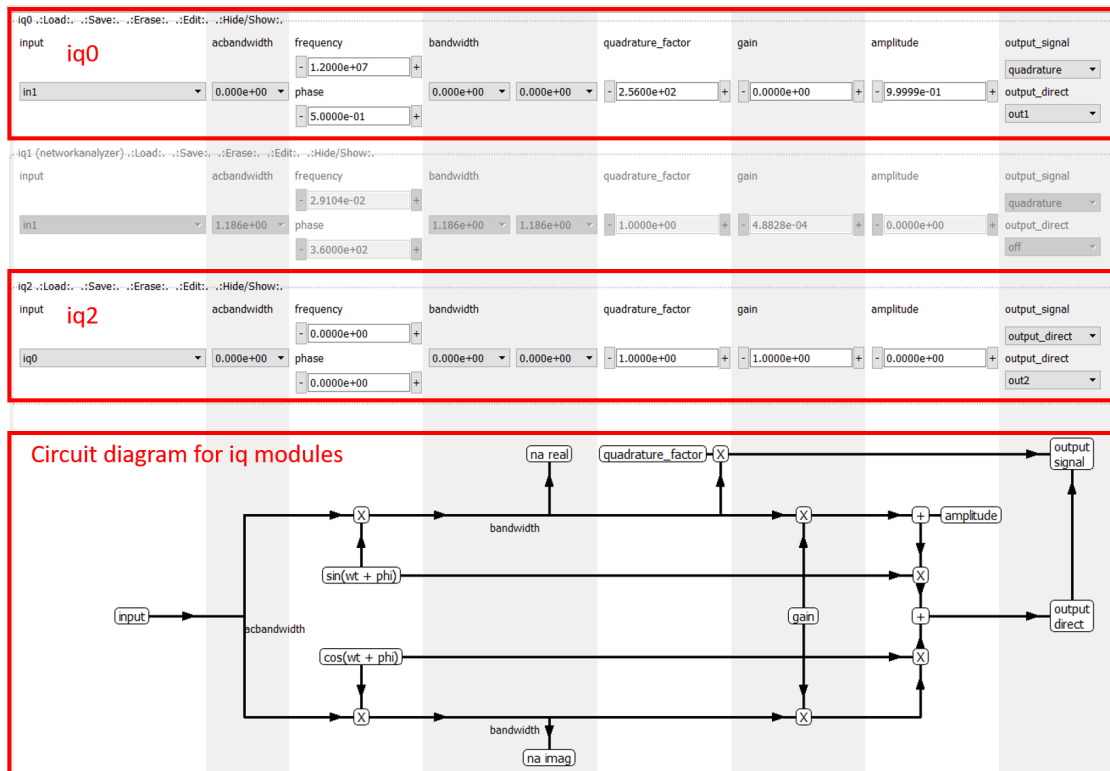


Figure 4.7: The GUI of the lock-in amplifier for the generating the modulation signal and the demodulation signal, involving two modules "iq0" and "iq2" originated from the IQ-modules template of PyRPL. For module "iq0", parameter "gain" is set to be 0 such that "output direct" becomes $\sin(\omega_m t + \phi)$ and is sent to "OUT1" for modulating the laser frequency. Module "iq2" takes the demodulation signal output of "iq0" and proceeds it to "OUT2" with parameter "gain" set to 1 and parameter "amplitude" set to 0.

4.1.3 Frequency locking on wavemeter

The frequency stabilization of the 399 nm laser and the 369 nm laser is realized on a standalone program¹³ based on the measurement done by our wavemeter. The program is written under Qt¹⁴, a software development kit that provides various built-in libraries especially for the development of GUI. It receives the measurement results of the wavemeter through UDP connection with the wavemeter client computer and performs PID feedback on the PZT voltage of the laser via an NI analog output device¹⁵ and subsequent amplifier¹⁶. The UDP connection is programmed with the QUdpSocket class of Qt and the development of controllable

¹³<https://github.com/wzl17/WMonitor/>

¹⁴<https://www.qt.io/>

¹⁵National Instrument NI6713.

¹⁶TEM-Messtechnik miniPiA 103, 3 Channel Piezo Amplifier.

analog output utilizes the built-in functions of NIDAQmx, the driver for NI devices.

As illustrated in Figure 4.8, for the frequency stabilization of a single laser, one complete laser frequency monitor and control unit is generated based on corresponding wavemeter channel and NI analog output channel given in the configuration file. This means an individual tab on the top for tracking the laser frequency and a parameter box for tuning the PZT voltage and PID settings of the lock. Due to limited wavemeter channels, the 399 nm laser and the 369 nm laser are sharing the same wavemeter channel at the moment, with a servo motor switch for switching between the signals of the two lasers. With this switching constantly on, it's possible to lock two lasers on the wavemeter at the same time when the frequency stability is not demanding. The control code for the servo motor shutters is given in Appendix B.



Figure 4.8: The WMonitor software for laser frequency stabilization on the wavemeter. The software contains five main components: frequency logging (yellow), interference pattern plotting (green), UDP connection control (blue), laser control (red) and shutter control (purple). The settings of these components can be modified in the configuration file (config.ini) attached to the program.

4.2 Trap voltage control

4.2.1 Master control program

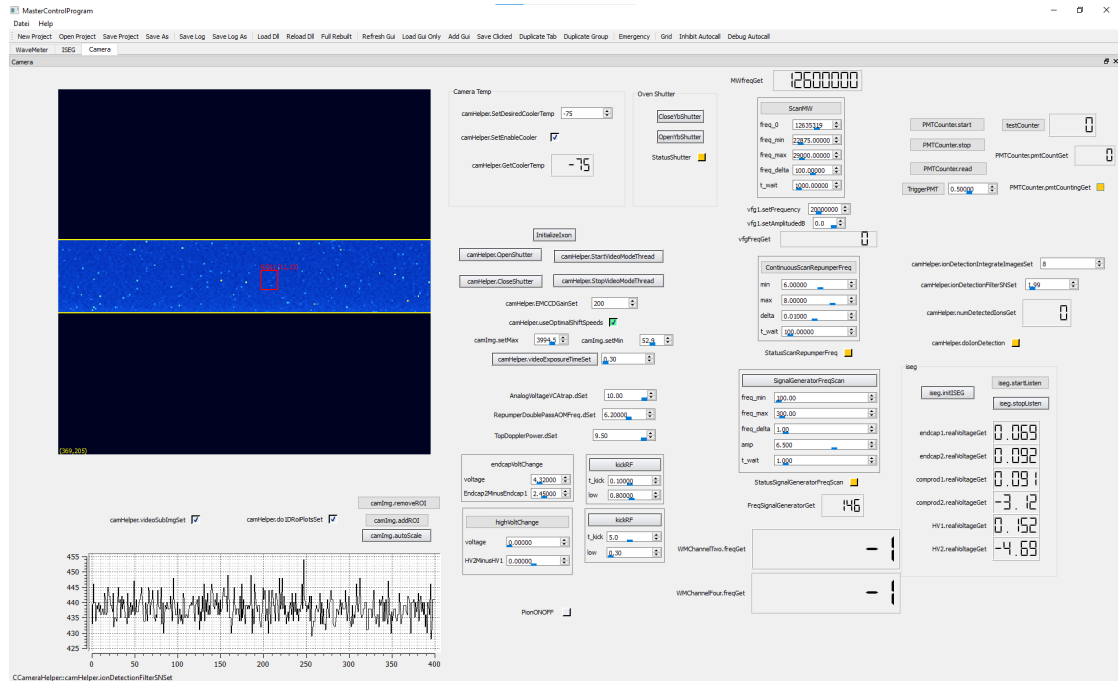


Figure 4.9: Overview of the current Master Control Program. At the start of the program or by clicking "reload DLL", the custom DLL project YbCrystalDll is compiled and loaded. The functions programmed inside can then be found in the right-click menu and can be placed anywhere on the GUI. The shape of the functions is adjusted automatically based on the parameter types and return types of the functions. Besides the GUI, the program contains a terminal where error messages are displayed.

The trap voltages control is realized through the Master Control Program (MCP), which is a C++ program developed by Kilian Singer at the University of Mainz. The program consists of three components: built-in libraries for controlling various hardware platforms including the camera and FPGA¹⁷, a library loader for loading external customized functions either dependent or independent on the built-in libraries, and a GUI showing the functions used for monitoring experimental parameters or system control. The customized functions for our experiment and corresponding libraries are programmed in a project called YbCrystalDll.

¹⁷FPGA "Bertha", developed in the University of Mainz.

4.2.2 Iseg module control

As discussed in Section 3.2.2, control of the RF voltage is realized by changing the control voltage of the VVA from the NI card analog output. It's thus straightforward to program this control in MCP based on its built-in support for the NI card. However, the built-in library of MCP does not support the network-based control of the Iseg module for controlling the DC voltages in the trap. To achieve this, custom library is programmed based on a library called `Websocket++`¹⁸ for network communication with the Iseg module.

To initialize the connection, the control program first sends a login request to the IP address of the Iseg module with username and password. After the module confirms the login by sending back a connection ID, the output channels of the module can be controlled by sending corresponding request. For instance, the output voltage of the channels can be changed and the channels can be set as open or closed. To read out the real-time output voltage of the channels, a request for reading needs to be sent, after which the module will start reporting the measured values continuously.

¹⁸<https://www.zaphoyd.com/projects/websocketpp/>.

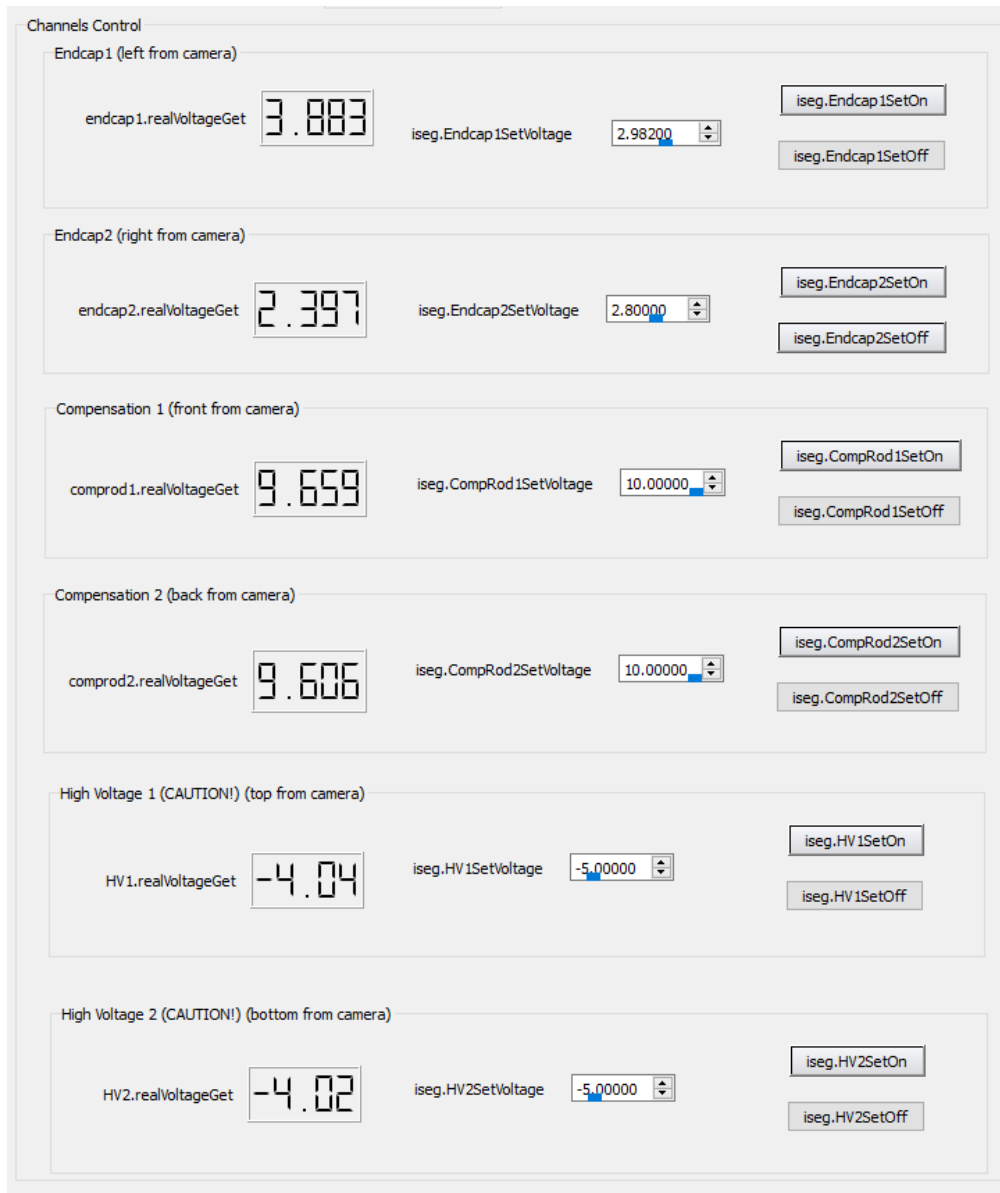


Figure 4.10: The functions for controlling the DC voltage on each electrode inside MCP.

Chapter 5

Trap Characterization

In this chapter, the preliminary characterizations that have been done on the setup will be presented. In Section 5.1, the measurement results of radial and axial trapping frequencies of the ions in the trap will be described. Based on the axial trapping frequency measurement, the magnification of the imaging system is analysed in Section 5.2. In Section 5.3, the effect of the high DC voltage for generating 2D ion crystal will be analyzed.

5.1 Trap frequency measurements

To measure the trapping frequency of the ions in the trap, an RF signal provided by a function generator¹ is coupled to one of DC electrodes using a 1 μ F capacitor. The frequency of this signal can be scanned from the MCP via serial port connection with the function generator. When the signal is on resonance with one of the ion's trapping frequencies, the corresponding oscillation of the ion can be excited, resulting in a drop in fluorescence.

For measuring the axial trapping frequency, the signal is sent to one of the endcaps. For radial trap frequency measurements, the signal is instead coupled to one of the micromotion compensation rods. The corresponding trap depth is varied respectively by changing the endcap voltages and the trap RF attenuation as shown in Figure 3.5, and the results are shown in Figure 5.1 and Figure 5.2.

¹Agilent 33250A

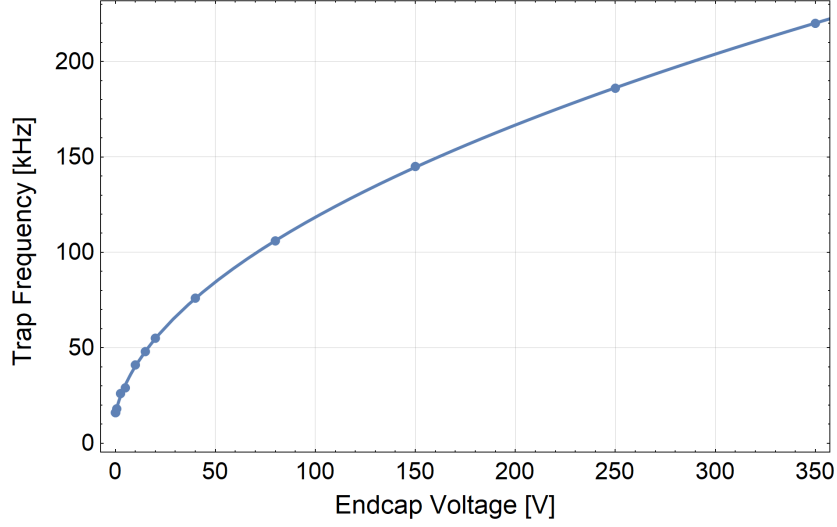


Figure 5.1: Measurement of the axial trap frequencies at different endcap voltages. The results are fitted to $f_z = \omega_z/(2\pi) = \Omega_{\text{rf}} \sqrt{\alpha_z^{\text{DC}} U_z + q_z^2/2}/(4\pi)$ with $\Omega_{\text{rf}} = 5.85$ MHz, showing $\alpha_z^{\text{DC}} = 1.610(8) \times 10^{-5} \text{V}^{-1}$ and $q_z = 0.0076(2)$. RF attenuation is set as 4.5 dB.

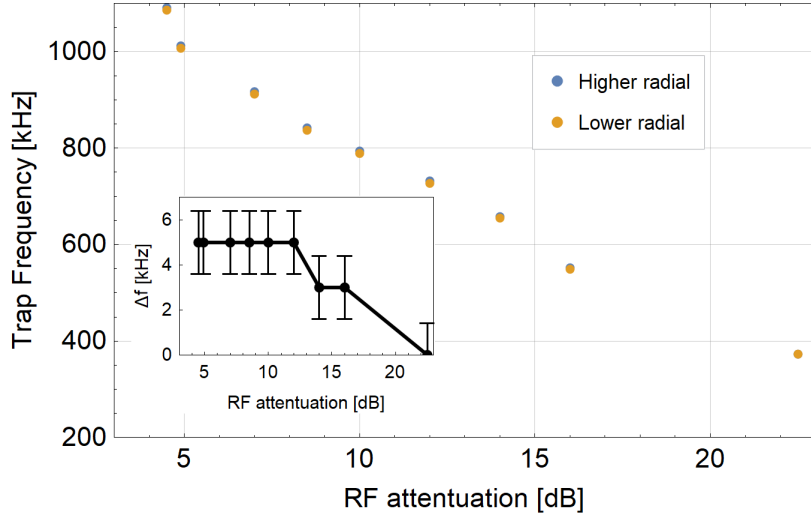


Figure 5.2: Measurement of the radial trap frequencies with different RF signal attenuation at the VVA. For each RF attenuation, two different radial frequencies can be measured which are shown in blue and orange, because small imperfections in the trap lift the degeneracy of the radial modes as shown in the inset. The measurement is done with endcap voltage set to 10 V and the maximum radial trap frequency is measured to be $2\pi \times 1.086$ MHz, corresponding to $q_{\text{max}} = 0.525$.

5.2 Magnification of imaging system

The axial trap frequency measurement is also used for estimating the magnification of the imaging system. For a given axial trap frequency, the distance L between ions in a 2-ion chain can be obtained from the equilibrium condition

$$m\omega_z^2 \frac{L}{2} = \frac{e^2}{4\pi\epsilon_0 L^2} \quad (5.1)$$

which gives $L = \sqrt[3]{e^2/(2\pi\epsilon_0 m\omega_z^2)}$. With the axial trap frequency ω_z set as $2\pi \times 29(1)$ kHz, the distance L can be calculated to be $36.4(8)$ μm and the image of a 2-ion crystal on the camera is shown in Figure 5.3. By fitting the ion positions assuming Gaussian distribution of the photon counts, the distance between the two ions on the camera can be calculated as $19.0(1)$ pixels. Since the pixel size is 16×16 μm^2 , the magnification of the imaging system $M = L_{\text{camera}}/L = 8.4(2)$.

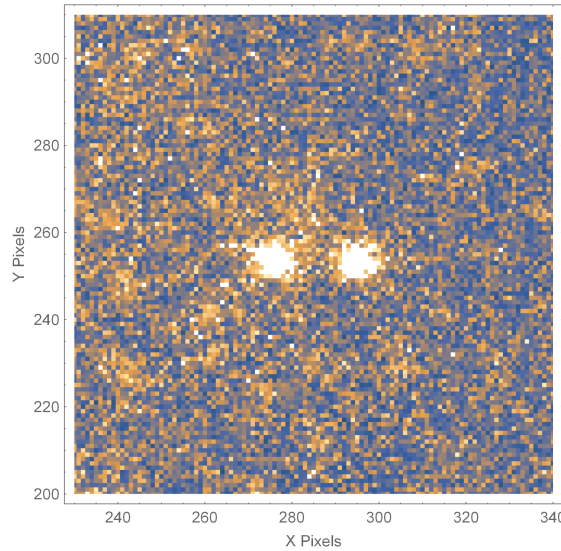


Figure 5.3: Camera image of a 2-ion chain.

5.3 Generation of 2D crystals

Based on trap frequency measurements, the effect of the DC high voltage electrodes for stretching ions from a 1D chain into a 2D crystal is also analysed. As shown in Figure 5.4, applying negative voltage $-U_{\text{hv}}$ on these electrodes generates an extra radial potential at the center of the trap given by

$$\Phi_{dc}^{rad} = \kappa_{\text{hv}}^{y'} U_{\text{hv}} y'^2 - \kappa_{\text{hv}}^{x'} U_{\text{hv}} x'^2 \quad (5.2)$$

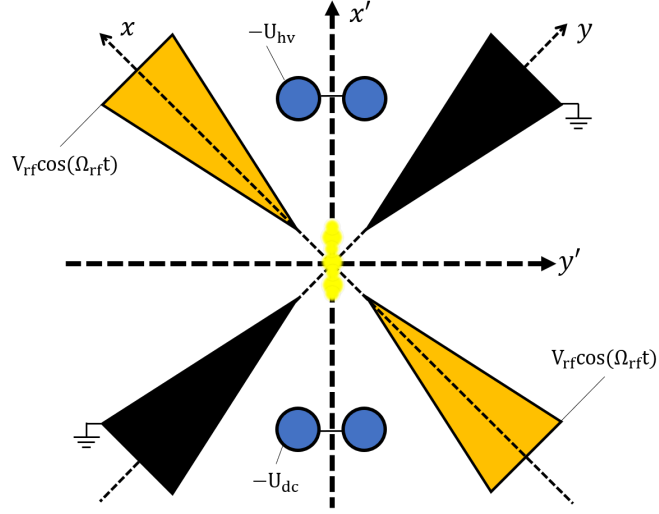


Figure 5.4: Schematics for the radial confinement of the ion crystal. The RF confining field is generated by applying RF signal on the orange blades and grounding the black blades. Negative DC voltage are supplied to the high voltage electrodes shown in blue circles for stretching the ions into a 2D plane shown in yellow.

where $\kappa_{\text{hv}}^{x',y'}$ are the geometrical factors of the high voltage electrodes along x' , y' directions. Based on Equation 2.7, this harmonic potential changes the radial trap frequencies of the ions to

$$\begin{aligned}\omega'_x &= \frac{\Omega_{\text{rf}}}{2} \sqrt{(a - \delta a_{x'}) + q^2/2}, \\ \omega'_y &= \frac{\Omega_{\text{rf}}}{2} \sqrt{(a + \delta a_{y'}) + q^2/2},\end{aligned}\tag{5.3}$$

where $\delta a_{x',y'} = 8e_0\kappa_{\text{hv}}^{x',y'} U_{\text{hv}}/(m\Omega_{\text{rf}}^2) = \alpha_{\text{hv}}^{x',y'} U_{\text{hv}}$ and we assume $a = a_1 \approx a_2$, $q = q_1 \approx -q_2$. In this way, the ion crystal is driven into a 2D plane perpendicular to the y' axis, as shown in Figure 5.5.

Figure 5.6 shows the measured radial trap frequencies in x' (in-plane) and y' (out of plane) directions. By fitting the results to Equation 5.3, the sensitivities of trap parameter a to the voltage on the high voltage electrodes are calculated to be $\alpha_{\text{hv}}^{x'} = 4.77(5) \times 10^{-6} \text{ V}^{-1}$ and $\alpha_{\text{hv}}^{y'} = 4.70(9) \times 10^{-6} \text{ V}^{-1}$.

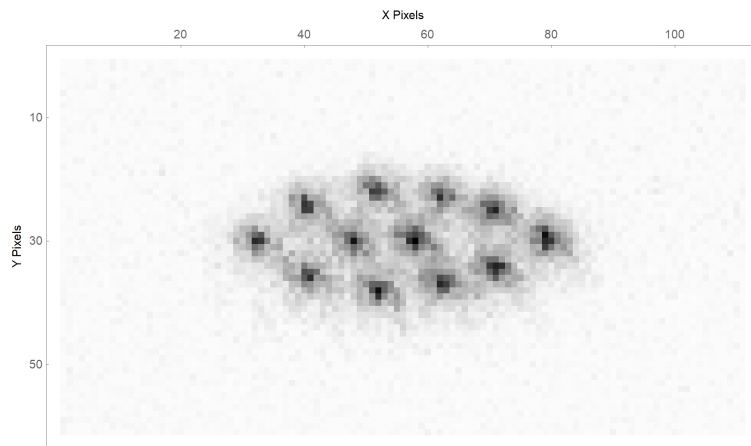


Figure 5.5: The image of a 2D ion crystal of 12 ions generated in the experiment.

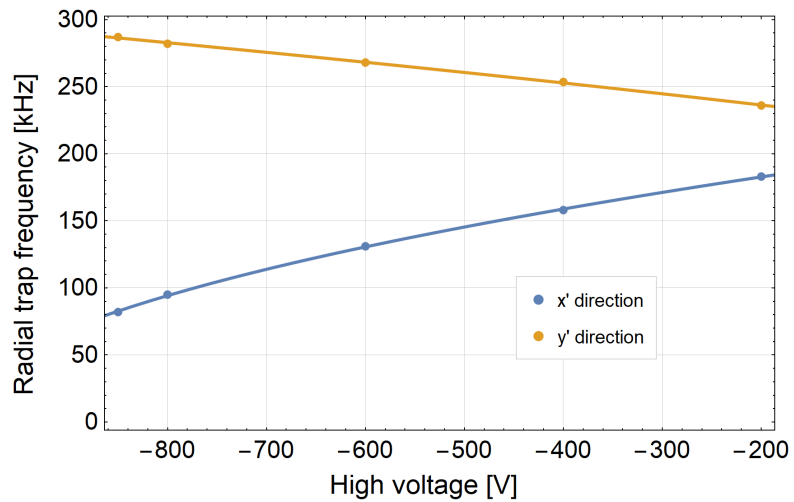


Figure 5.6: Trap frequencies along x' and y' directions measured with different negative voltages applied to high voltage electrodes. As the amplitude of the voltage increases, the confinement along the y' direction increases the confinement along the x' direction decreases to the level of the axial confinement. Ions are thus strongly confined in the the y' direction and spread in the $x'z$ plane to form a 2D crystal.

Chapter 6

Conclusion and Outlook

In this thesis, the experimental setup that has been built for quantum simulation with trapped ions in optical tweezers is described. In the setup, a quadrupole ion trap is installed in a vacuum chamber with the voltages for generating the confining potential well controlled. For generating of the Yb^+ ions with photoionization and Doppler cooling the ions, several laser systems are built with their frequencies stabilized to an optical reference cavity or a wavemeter. The laser cooled ions are observed using a EMCCD camera with the imaging system. Optical tweezers generated by a spatial light modulator can also be sent to the ions through the imaging path. Based on the experimental setup, trap frequencies of the ions confined in the trap are measured for trap characterization and 2D ion crystal of $^{174}\text{Yb}^+$ ions can be successfully created.

The next step of the experiment will be trapping $^{171}\text{Yb}^+$ ions with the hyperfine qubit states, which requires the implementation of a 12.6 GHz microwave signal driving the qubit transition and appropriate magnetic field using permanent magnets for lifting the degeneracy of the hyperfine manifolds. After the implementation of Sisyphus cooling or EIT cooling that cools the ions into the Lamb-Dicke regime, the generation of the spin-spin interaction can be performed using a 368 nm Raman laser. For tuning the spin-spin interaction, the optical tweezers need to align to the ions with the stabilized pinning potential. This can be done by applying the 935 nm or 760 nm repumper laser in the optical path of the tweezer light for initial alignment and by supplying near-resonant oscillating electric field on the ions to probe the change in trapping frequency brought by the tweezers.

Appendix A

ECDL Circuits

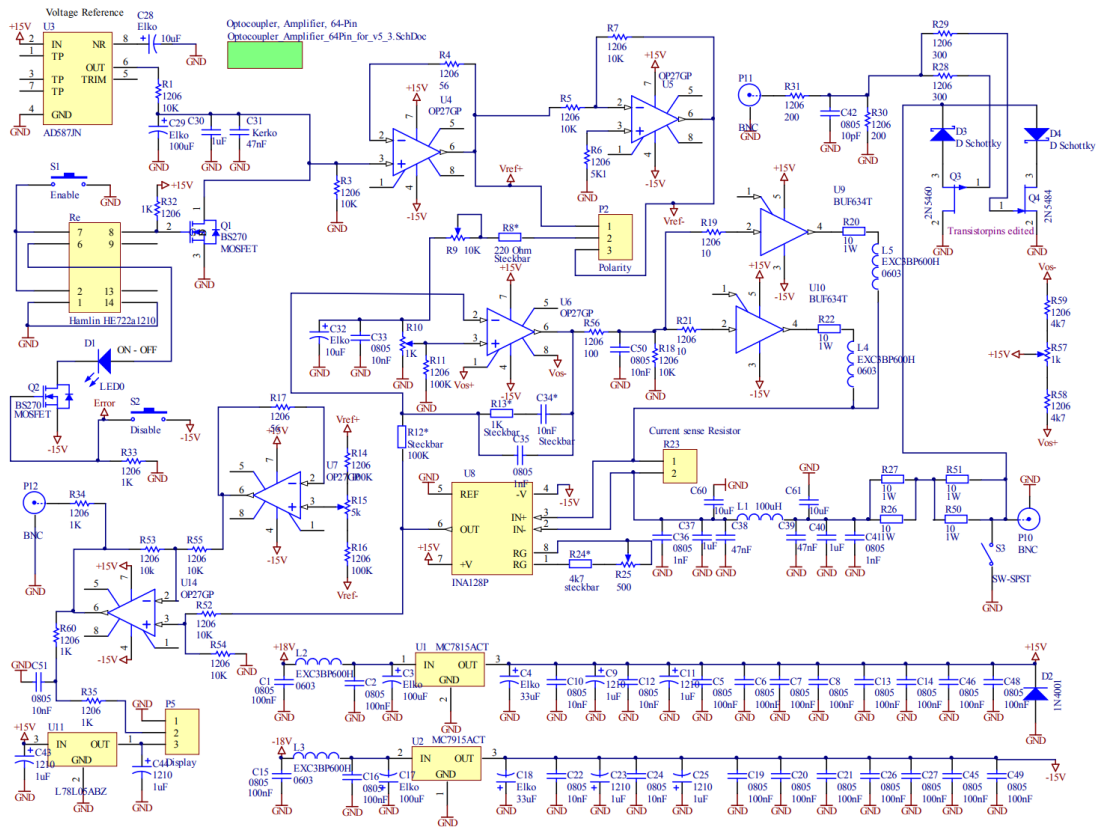


Figure A.1: Current driver for the 399 nm diode laser from [38].

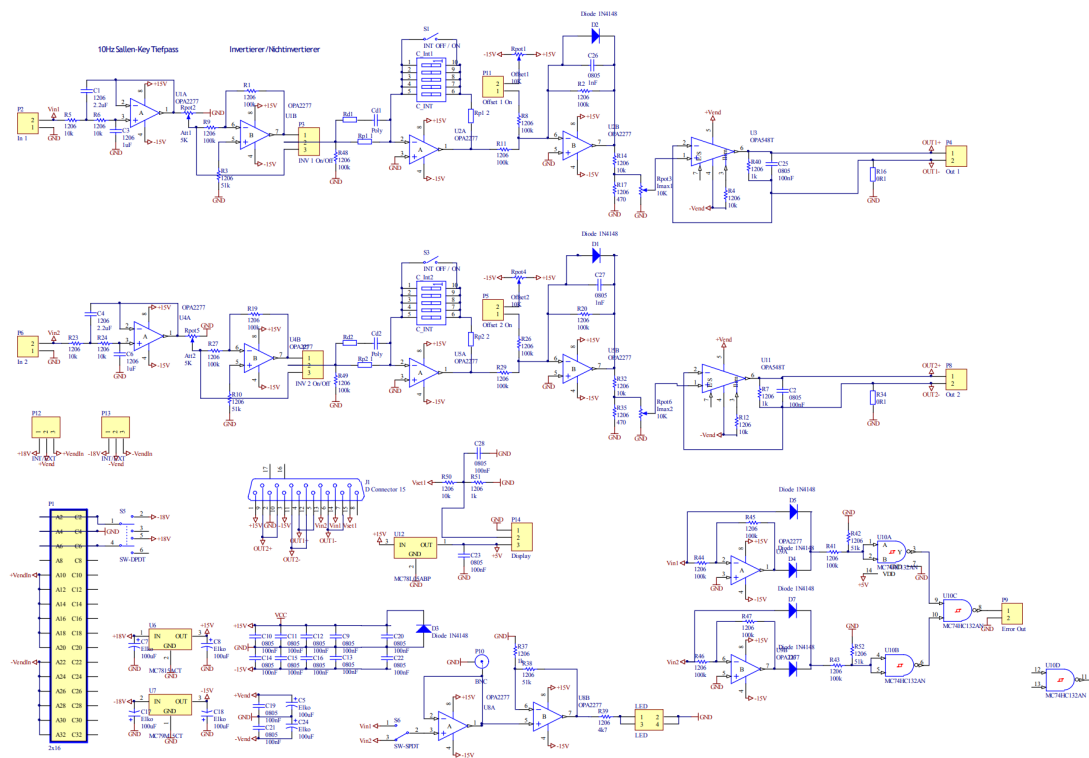


Figure A.2: Temperature stabilization circuits for the 399 nm diode laser from [38]. It contains two individual PID modules for stabilizing both the temperature of the laser diode and that of the laser enclosure based on the corresponding error signals given by two thermistors.

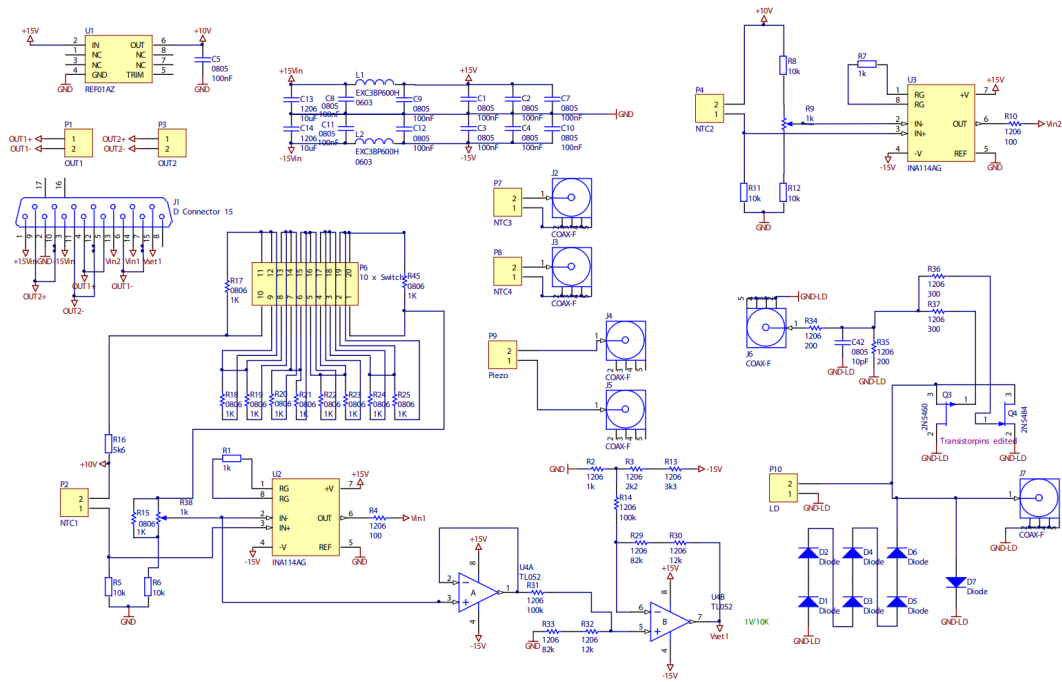


Figure A.3: Temperature sensing circuits and the laser diode protection circuit for the 399 nm diode laser from [38]. The target temperatures of the laser diode and the enclosure are respectively probed by thermistor NTC1 and NTC2. The changes in the temperatures are reflected in changes in the voltages on the thermistors, which are compared to the setpoint voltages. The voltage differences are then amplified and sent as Vin1 and Vin2 to the temperature stabilization circuits which produce the feedback signals for driving the Peltier modules connected to P1 and P2. NTC3 and NTC4 are not in used.

Appendix B

Shutter Control Codes

The Arduino code for controlling the servo motor shutter in the experiment:

```
1 // ref: https://github.com/adafruit/Adafruit-PWM-Servo-Driver-Library
2 // Based on: https://rootsaid.com/pca9685-servo-driver/
3 // Motor shutter for laser beams
4 // Multi-control server: PCA9685
5 // I2C control via arduino Uno
6 // Motor servo: SG90
7 // PWM Period: 20 ms (50Hz); Duty Cycle: 1-2 ms
8
9 #include <Wire.h>
10 #include <Adafruit_PWMServoDriver.h>
11
12 Adafruit_PWMServoDriver pwm = Adafruit_PWMServoDriver();
13
14 #define MIN_DUTY_WIDTH 200 //min duty time ~1 ms
15 #define MAX_DUTY_WIDTH 450 //max duty time ~2 ms
16 #define DEFAULT_DUTY_WIDTH 307 //default duty time 1.5 ms
17 #define PERIOD_WIDTH 4096
18 #define FREQUENCY 50
19
20 // up to 16 servo controlled by PWM output pins labeled 0~15
21 uint8_t servonum = 0;
22 int pwm_ON = 409;
23 int pwm_OFF_A = pwm_ON + MIN_DUTY_WIDTH/2;
24 int pwm_OFF_B = pwm_ON + MAX_DUTY_WIDTH/2;
25 int pwm_OFF_0 = pwm_ON + DEFAULT_DUTY_WIDTH;
26 int pwmState = pwm_OFF_A;
27 int switchState = LOW;
28 String sdata = "";
29 char ch;
30 const long interval = 1000; // unit time of switching
31 long interval_A = 5000;
32 long interval_B = 5000;
33 unsigned long previousMillis = 0;
34
35 void ShutterPos0(uint8_t servo_n) {
36   pwm.setPWM(servo_n, pwm_ON, pwm_OFF_0);
37 }
38
39 void setup()
40 {
41   Serial.begin(9600);
42   //Serial.println("Connected! shutters in operation");
43   pwm.begin();
44   pwm.setPWMPfreq(FREQUENCY);
45   int i;
46   for ( i = 0; i < 16; i++ )
47     ShutterPos0(i);
48 }
49
50 void loop() {
51   while (Serial.available() > 0) {
52     ch = Serial.read();
53     if (ch=='\n') {
54       delay(50);
55       Serial.print("Receive:");
```

```

56     Serial.println(sdata); //in the form of "servo01 to C(1,2)" where 1 and 2 are the time on each state
57     delay(50);
58     servonum = (sdata[5]-'0')*10 + (sdata[6]-'0');
59     if (servonum < 0 || servonum > 15 || sdata.length()!=17)
60         Serial.println("Invalid_command!");
61     else if (sdata[11]=='C') {
62         if ( (sdata[13]-'0')>0 && (sdata[13]-'0')<=9 )
63             interval_A = (sdata[13]-'0')*interval;
64         if ( (sdata[15]-'0')>0 && (sdata[15]-'0')<=9 )
65             interval_B = (sdata[15]-'0')*interval;
66         switchState = HIGH;
67         Serial.println("Switching_on.");
68     }
69     else if (sdata[11]=='D') {
70         switchState = LOW;
71         Serial.println("Switching_off.");
72     }
73     else if (sdata[11]=='A') {
74         switchState = LOW;
75         pwm.setPWM(servonum, pwm_ON, pwm_OFF_A);
76         Serial.println("Switched_to_A.");
77     }
78     else if (sdata[11]=='B') {
79         switchState = LOW;
80         pwm.setPWM(servonum, pwm_ON, pwm_OFF_B);
81         Serial.println("Switched_to_B.");
82     }
83     else Serial.println("Invalid_command!");
84     sdata = "";
85 }
86 else sdata += (char)ch;
87 }
88 if (switchState == HIGH) {
89     unsigned long currentMillis = millis();
90     if (pwmState == pwm_OFF_A) {
91         if (currentMillis - previousMillis >= interval_A) {
92             previousMillis = currentMillis;
93             pwmState = pwm_OFF_B;
94             pwm.setPWM(servonum, pwm_ON, pwmState);
95         }
96     }
97     else if (pwmState == pwm_OFF_B) {
98         if (currentMillis - previousMillis >= interval_B) {
99             previousMillis = currentMillis;
100            pwmState = pwm_OFF_A;
101            pwm.setPWM(servonum, pwm_ON, pwmState);
102        }
103    }
104 }
105 }

```

Bibliography

- ¹Y. Cao, J. Romero, and A. Aspuru-Guzik, “Potential of quantum computing for drug discovery”, *IBM Journal of Research and Development* **62**, 6:1–6:20 (2018).
- ²B. Bauer, S. Bravyi, M. Motta, and G. K.-L. Chan, “Quantum Algorithms for Quantum Chemistry and Quantum Materials Science”, *Chemical Reviews* **120**, 12685–12717 (2020).
- ³J. I. Cirac and P. Zoller, “Goals and opportunities in quantum simulation”, en, *Nature Physics* **8**, 264–266 (2012).
- ⁴I. M. Georgescu, S. Ashhab, and F. Nori, “Quantum Simulation”, en, *Reviews of Modern Physics* **86**, 153–185 (2014).
- ⁵M. A. Nielsen and I. Chuang, *Quantum computation and quantum information* (American Association of Physics Teachers, 2002).
- ⁶D. Gottesman, “Fault-Tolerant Quantum Computation with Constant Overhead”, arXiv:1310.2984 [quant-ph] (2014).
- ⁷B. M. Terhal, “Quantum error correction for quantum memories”, en, *Reviews of Modern Physics* **87**, 307–346 (2015).
- ⁸Z. Chen, K. J. Satzinger, J. Atalaya, A. N. Korotkov, A. Dunsworth, D. Sank, C. Quintana, M. McEwen, R. Barends, P. V. Klimov, S. Hong, C. Jones, A. Petukhov, D. Kafri, S. Demura, B. Burkett, C. Gidney, A. G. Fowler, A. Paler, H. Putterman, I. Aleiner, F. Arute, K. Arya, R. Babbush, J. C. Bardin, A. Bengtsson, A. Bourassa, M. Broughton, B. B. Buckley, D. A. Buell, N. Bushnell, B. Chiaro, R. Collins, W. Courtney, A. R. Derk, D. Eppens, C. Erickson, E. Farhi, B. Foxen, M. Giustina, A. Greene, J. A. Gross, M. P. Harrigan, S. D. Harrington, J. Hilton, A. Ho, T. Huang, W. J. Huggins, L. B. Ioffe, S. V. Isakov, E. Jeffrey, Z. Jiang, K. Kechedzhi, S. Kim, A. Kitaev, F. Kostritsa, D. Landhuis, P. Laptev, E. Lucero, O. Martin, J. R. McClean, T. McCourt, X. Mi, K. C. Miao, M. Mohseni, S. Montazeri, W. Mruczkiewicz, J. Mutus, O. Naaman, M. Neeley, C. Neill, M. Newman, M. Y. Niu, T. E. O’Brien, A. Opremcak, E. Ostby, B. Pató, N. Redd, P. Roushan, N. C. Rubin, V. Shvarts, D. Strain, M. Szalay, M. D. Trevithick, B. Villalonga, T. White, Z. J. Yao, P. Yeh, J. Yoo, A. Zalcman, H. Neven, S. Boixo, V. Smelyanskiy, Y. Chen, A. Megrant,

- J. Kelly, and Google Quantum AI, “Exponential suppression of bit or phase errors with cyclic error correction”, en, *Nature* **595**, 383–387 (2021).
- ⁹R. P. Feynman, “Simulating Physics with Computers”, *International Journal of Theoretical Physics* **21**, 467–488 (1982).
- ¹⁰R. Blatt and C. F. Roos, “Quantum simulations with trapped ions”, en, *Nature Physics* **8**, 277–284 (2012).
- ¹¹J. I. Cirac and P. Zoller, “Quantum Computations with Cold Trapped Ions”, en, *Physical Review Letters* **74**, 4091–4094 (1995).
- ¹²D. Wineland, C. Monroe, W. Itano, D. Leibfried, B. King, and D. Meekhof, “Experimental issues in coherent quantum-state manipulation of trapped atomic ions”, en, *Journal of Research of the National Institute of Standards and Technology* **103**, 259 (1998).
- ¹³A. Sørensen and K. Mølmer, “Quantum computation with ions in thermal motion”, *Physical Review Letters* **82**, 1971 (1999).
- ¹⁴J. M. Pino, J. M. Dreiling, C. Figgatt, J. P. Gaebler, S. A. Moses, M. S. Allman, C. H. Baldwin, M. Foss-Feig, D. Hayes, K. Mayer, C. Ryan-Anderson, and B. Neyenhuis, “Demonstration of the trapped-ion quantum CCD computer architecture”, en, *Nature* **592**, 209–213 (2021).
- ¹⁵K. Kim, M.-S. Chang, S. Korenblit, R. Islam, E. E. Edwards, J. K. Freericks, G.-D. Lin, L.-M. Duan, and C. Monroe, “Quantum simulation of frustrated Ising spins with trapped ions”, en, *Nature* **465**, 590–593 (2010).
- ¹⁶K. Kim, S. Korenblit, R. Islam, E. E. Edwards, M.-S. Chang, C. Noh, H. Carmichael, G.-D. Lin, L.-M. Duan, C. C. J. Wang, J. K. Freericks, and C. Monroe, “Quantum simulation of the transverse Ising model with trapped ions”, *English, New Journal of Physics* **13**, 105003 (2011).
- ¹⁷J. W. Britton, B. C. Sawyer, A. C. Keith, C.-C. J. Wang, J. K. Freericks, H. Uys, M. J. Biercuk, and J. J. Bollinger, “Engineered two-dimensional Ising interactions in a trapped-ion quantum simulator with hundreds of spins”, en, *Nature* **484**, 489–492 (2012).
- ¹⁸J. Zhang, G. Pagano, P. W. Hess, A. Kyprianidis, P. Becker, H. Kaplan, A. V. Gorshkov, Z.-X. Gong, and C. Monroe, “Observation of a many-body dynamical phase transition with a 53-qubit quantum simulator”, en, *Nature* **551**, 601–604 (2017).
- ¹⁹K. Kim, M.-S. Chang, R. Islam, S. Korenblit, L.-M. Duan, and C. Monroe, “Entanglement and Tunable Spin-Spin Couplings between Trapped Ions Using Multiple Transverse Modes”, en, *Physical Review Letters* **103**, 120502 (2009).

- ²⁰J. D. Arias Espinoza, M. Mazzanti, K. Fouka, R. X. Schuessler, Z. Wu, P. Corboz, R. Gerritsma, and A. Safavi-Naini, “Engineering spin-spin interactions with optical tweezers in trapped ions”, English, *Physical Review A* **104**, 013302 (2021).
- ²¹S. Earnshaw, “On the Nature of the Molecular Forces which Regulate the Constitution of the Luminiferous Ether”, *Transactions of the Cambridge Philosophical Society* **7**, 97 (1848).
- ²²W. Paul, “Electromagnetic traps for charged and neutral particles”, en, *Reviews of Modern Physics* **62**, 531–540 (1990).
- ²³H. A. FÜRST, “Trapped ions in a bath of ultracold atoms”, PhD thesis (University of Amsterdam, 2019).
- ²⁴N. V. Ewald, “Ultracold Rydberg atoms interacting with trapped ions”, en, PhD thesis (University of Amsterdam, 2021).
- ²⁵S. Mulholland, H. A. Klein, G. P. Barwood, S. Donnellan, P. B. R. Nisbet-Jones, G. Huang, G. Walsh, P. E. G. Baird, and P. Gill, “Compact laser system for a laser-cooled ytterbium ion microwave frequency standard”, *Review of Scientific Instruments* **90**, 033105 (2019).
- ²⁶R. W. Berends, E. H. Pinnington, B. Guo, and Q. Ji, “Beam-laser lifetime measurements for four resonance levels of Yb II”, en, *Journal of Physics B: Atomic, Molecular and Optical Physics* **26**, L701–L704 (1993).
- ²⁷R. Lange, A. A. Peshkov, N. Huntemann, C. Tamm, A. Surzhykov, and E. Peik, “Lifetime of the $^2F_{7/2}$ level in Yb^+ for spontaneous emission of electric octupole radiation”, arXiv:2107.11229 [physics, physics:quant-ph] (2021).
- ²⁸Jannis Klaus Joger, “Cold Li–Yb+ mixtures in a hybrid trap setup”, PhD thesis (University of Amsterdam, 2018).
- ²⁹K. R. Islam, “Quantum simulation of interacting spin models with trapped ions”, PhD thesis (University of Maryland, 2012).
- ³⁰D. James, “Quantum dynamics of cold trapped ions with application to quantum computation”, en, *Applied Physics B: Lasers and Optics* **66**, 181–190 (1998).
- ³¹R. Nath, M. Dalmonte, A. W. Glaetzle, P. Zoller, F. Schmidt-Kaler, and R. Gerritsma, “Hexagonal plaquette spin–spin interactions and quantum magnetism in a two-dimensional ion crystal”, en, *New Journal of Physics* **17**, 065018 (2015).
- ³²A. Bermudez, J. Almeida, F. Schmidt-Kaler, A. Retzker, and M. B. Plenio, “Frustrated Quantum Spin Models with Cold Coulomb Crystals”, *Physical Review Letters* **107**, 207209 (2011).

- ³³A. Bermudez, J. Almeida, K. Ott, H. Kaufmann, S. Ulm, U. Poschinger, F. Schmidt-Kaler, A. Retzker, and M. B. Plenio, “Quantum magnetism of spin-ladder compounds with trapped-ion crystals”, en, *New Journal of Physics* **14**, 093042 (2012).
- ³⁴J. D. Siverns, L. R. Simkins, S. Weidt, and W. K. Hensinger, “On the application of radio frequency voltages to ion traps via helical resonators”, *Applied Physics B* **107**, 921–934 (2012).
- ³⁵M. Johanning, A. Braun, D. Eiteneuer, C. Paape, C. Balzer, W. Neuhauser, and C. Wunderlich, “Resonance-enhanced isotope-selective photoionization of YbI for ion trap loading”, en, *Applied Physics B* **103**, 327–338 (2011).
- ³⁶D. Das, S. Barthwal, A. Banerjee, and V. Natarajan, “Absolute frequency measurements in Yb with 0.08 ppb uncertainty: Isotope shifts and hyperfine structure in the 399-nm $S_{0}P_{1}$ line”, *Physical Review A* **72**, 032506 (2005).
- ³⁷S. Botsi, “Design and Construction of two External-Cavity Diode Lasers for Rydberg excitation of Rb atoms”, Bachelor’s thesis (University of Amsterdam, June 2014).
- ³⁸M. J. Mark, “Experiments with tunable quantum gases in optical lattices”, PhD thesis (University of Innsbruck, 2012).
- ³⁹S. Ejtemaee and P. C. Haljan, “3D Sisyphus Cooling of Trapped Ions”, *Physical Review Letters* **119**, 043001 (2017).
- ⁴⁰M. Qiao, Y. Wang, Z. Cai, B. Du, P. Wang, C. Luan, W. Chen, H.-R. Noh, and K. Kim, “Double-Electromagnetically-Induced-Transparency Ground-State Cooling of Stationary Two-Dimensional Ion Crystals”, *Physical Review Letters* **126**, 023604 (2021).
- ⁴¹L. Feng, W. L. Tan, A. De, A. Menon, A. Chu, G. Pagano, and C. Monroe, “Efficient Ground-State Cooling of Large Trapped-Ion Chains with an Electromagnetically-Induced-Transparency Tripod Scheme”, en, *Physical Review Letters* **125**, 053001 (2020).
- ⁴²T. Tiecke, “Feshbach resonances in ultracold mixtures of the fermionic quantum gases”, PhD Thesis (University of Amsterdam, 2009).
- ⁴³Z. Zhou, B. Pain, and E. Fossum, “Frame-transfer CMOS active pixel sensor with pixel binning”, *IEEE Transactions on Electron Devices* **44**, 1764–1768 (1997).
- ⁴⁴R. M. W. van Bijnen, “Quantum engineering with ultracold atoms”, PhD Thesis (Citeseer, 2013).
- ⁴⁵E. D. Black, “An introduction to Pound–Drever–Hall laser frequency stabilization”, *American Journal of Physics* **69**, 79–87 (2001).

⁴⁶M. A. Luda, M. Drechsler, C. T. Schmiegelow, and J. Codnia, “Compact embedded device for lock-in measurements and experiment active control”, *Review of Scientific Instruments* **90**, 023106 (2019).